New advances in using seismic anisotropy, mineral physics and geodynamics to understand deformation in the lowermost mantle

Andy Nowacki*, James Wookey, J-Michael Kendall

School of Earth Sciences, University of Bristol, Wills Memorial Building, Queen's Road, Bristol, BS8 1RJ, UK

Abstract

The D″ region, which lies in the lowermost few hundred kilometres of the mantle, is a central cog in the Earth's heat engine, influencing convection in the underlying core and overlying mantle. In recent years dense seismic networks have revealed a wealth of information about the seismic properties of this region, which are distinct from those of the mantle above. Here we review observations of seismic anisotropy in this region. In the past it has been assumed that the region exhibits a simple form of transverse isotropy with a vertical symmetry axis (VTI anisotropy). We summarise new methodologies for characterising a more general style of anisotropy using observations from a range of azimuths. The observations can be then used to constrain the mineralogy of the region and its style of deformation by a lattice preferred orientation (LPO) of the constituent minerals. Of specific interest is the recent discovery of the stability of the post-perovskite phase in this region, which might explain many enigmatic properties of D″. Mantle flow models based on density models derived from global tomographic seismic velocity models can be used to test plausible mineralogies, such as post-perovskite, and their deformation mechanisms. Here we show how linked predictions from mineral physics, geodynamical modelling and seismic observations can be used to better constrain the dynamics, mineralogy and physical properties of the lowermost mantle.

Keywords: D″, lowermost mantle, mantle flow, anisotropy

1. Introduction

1.1. D″ and the lowermost mantle

The primary evidence for stratification of the Earth's interior comes from seismology. For nearly three quarters of a century seismologists have used changes in velocity gradients to map out the concentric shells that constitute the Earth's interior. Some changes are dramatic, like that seen at the core-mantle boundary (CMB), whilst others are more subtle,

*Corresponding author.
Email address: andy.nowacki@bristol.ac.uk (Andy Nowacki)

like that seen at the base of the lithosphere. Not long after Bullen's (1940) original classification of the lower mantle as the 'D' layer, it became apparent that the bottom few hundred kilometres of the mantle were seismically distinct from the bulk of the lower mantle. The lower mantle was split into D′—the top—and D″—the bottom (Bullen, 1949). Whilst much of the original nomenclature used to label the layers of the Earth has been abandoned, D″ retains the name given to it over 60 years ago.

The D″ region encompasses a thermal boundary layer between the hot and vigorously convecting outer core and the colder, more slowly convecting mantle. It marks the terminus of downwelling mantle material and the place where upwelling plumes most probably originate. It is often bounded by a seismic discontinuity that lies on average 250 km above the CMB (*e.g.*, Wysession et al., 1998), in many places contains ultra-low velocity zones at its base (*e.g.*, Garnero et al., 1998), and generally exhibits fine-scale structure revealed through scattered seismic energy (*e.g.*, Hedlin et al., 1997). The focus of this review is the observation and interpretation of seismic anisotropy in this regio: in contrast to the overlying lower mantle, it exhibits significant seismic anisotropy (Meade et al., 1995; Montagner and Kennett, 1996; Panning and Romanowicz, 2006)

The implications of these observations are far reaching, as the CMB region plays a fundamental role in the dynamics of the mantle above and the core below. For example, core convection controls the generation of the Earth's magnetic field; mantle convection is the driving force behind plate tectonics. Making sense of the seismic observations requires a linked analysis of mineral physics, geodynamics and seismology. Here we present recent advances in each of these fields and show how they can be used to constrain the interpretation of measurements of seismic anisotropy.

1.2. Seismic anisotropy

Seismic anisotropy—the variation of seismic wave speed with direction—appears to be commonplace in the upper- and lowermost mantle (see *e.g.* Savage, 1999), and is probably present in the inner core (for a review, see Tromp, 2001). Anisotropy may be related to the inherent, wavelength-independent nature of the medium through which a wave travels, such as within the crystal structure of many minerals in the Earth; or it may be due to extrinsic, wavelength-dependent ordering of heterogeneous material, such as sedimentary layering in basins. In either case, the propagation of an elastic wave through the medium is described by the elasticity tensor.

The elasticity tensor c_{ijkl} gives the relationship between the applied stress σ_{ij} and the resulting strain ϵ_{kl} according to a linear relationship (Hooke's Law $\sigma_{ij} = c_{ijkl}\,\epsilon_{kl}$; for instance, see Nye, 1985 or Hudson, 1980a). The infinitesimal strain is

$$\epsilon_{kl} = \frac{1}{2}\left(\frac{\partial u_k}{\partial x_l} + \frac{\partial u_l}{\partial x_k}\right) ,$$

where u_n is displacement and x_n is the corresponding cartesian direction. The $3\times3\times3\times3$ c_{ijkl} tensor can be reduced by symmetry ($\sigma_{ij} = \sigma_{ji}$) to a 6×6 matrix using the Voigt notation,

$$ij \rightarrow i,\ kl \rightarrow j,\ c_{ijkl} \rightarrow C_{ij},$$

$$Cij = \begin{bmatrix} C_{11} & C_{12} & C_{13} & C_{14} & C_{15} & C_{16} \\ & C_{22} & C_{23} & C_{24} & C_{25} & C_{26} \\ & & C_{33} & C_{34} & C_{35} & C_{36} \\ & & & C_{44} & C_{45} & C_{46} \\ & & & & C_{55} & C_{56} \\ & & & & & C_{66} \end{bmatrix} .$$

The matrix is symmetrical, hence the lower elements are not shown, and there are 21 independent elastic constants which describe a minimally symmetrical, fully anisotropic system, an example of which would be a triclinic crystal. Increasing symmetry within a system reduces the number of independent elastic constants. For orthorhombic symmetries, there are nine; for hexagonal symmetry, there are five (C_{11}, C_{33}, C_{44}, C_{66} and C_{13}); for cubic there are three (C_{11}, C_{44} and C_{12}); and for isotropic media, there are only two (C_{11} and C_{44}). (For this special case, $C_{11} = C_{22} = C_{33}$, $C_{12} = C_{13} = C_{23}$, and $C_{44} = C_{55} = C_{66} = (C_{11} - C_{12})/2$.) A visual summary of the independent terms in the matrix C_{ij} for each crystal symmetry class can be found on p. 148 in Royer and Dieulesaint (2000).

Because the full tensor is so complicated, it is usual to make assumptions about the kind of symmetry present in the Earth; hexagonal symmetries are a good approximation where sedimentary layering or oriented cracks or inclusions are present. Where the layering is horizontal, the hexagonal symmetry can be described by a vertical axis of rotational symmetry; if it is inclined, then so is the symmetry axis (Figure 1). The plane normal to the symmetry axis is the plane of isotropy. When the plane of isotropy is horizontal (the axis of symmetry vertical), this is often referred to as vertical transverse isotropy (VTI), whereas a more general case where the plane inclined is termed tilted transverse isotropy (TTI).

In order to calculate the phase velocity along any particular direction given an elastic tensor, one solves the Christoffel equation,

$$\det|c_{ijkl}\, n_i\, n_j - \rho v_n^2\, \delta_{il}| = 0 \ ,$$

where n_i is the unit normal to the plane wavefront, ρ is the density, v_n is the phase velocity along the plane wavefront normal, and δ is the Kronecker delta. The three eigenvalues of the solution correspond to the P and S wave velocities, V_{P}, V_{S1} and V_{S2}, along this direction (strictly, to the phase velocities of the quasi-compressional and -shear waves, which are not necessarily parallel and orthogonal respectively to n_i).

1.3. Shear wave splitting

Shear wave splitting occurs when a transverse wave travels through an anisotropic medium. Analogous to optic birefringence, this creates two orthogonally-polarised waves (the fast wave, S_1 and slow, S_2) (Figure 2). Depending on the distance travelled in the anisotropic medium, s, and the two velocities, V_{S1} and V_{S2}, the slow wave will be delayed by some time $\delta t = s\left(\frac{1}{V_{\mathrm{S2}}} - \frac{1}{V_{\mathrm{S1}}}\right)$. The measured polarisation of S_1 is termed the fast orientation, ϕ, and this is measured at the seismic station, hence ϕ is usually in the geographic frame and measured as an azimuth from north. The fast orientation in the ray frame, ϕ', is measured relative to the intersection between the Earth radial plane (vertical) and the ray normal plane, and therefore ϕ' is constant whilst the ray is not being actively split in an anisotropic region.

The strength of the S-wave anisotropy along a certain direction in the anisotropic medium is generally expressed as $\delta V_{\mathrm{S}} = 2(V_{\mathrm{S1}} - V_{\mathrm{S2}})/(V_{\mathrm{S1}} + V_{\mathrm{S2}}) \approx (V_{\mathrm{S}}\,\delta t)/s$. Hence in making measurements of splitting, normally one must assume a background 'average' V_{S} (from global 1–D or tomographic models) and distance travelled in the anisotropic region, in order to calculate δV_{S}, with these uncertainties inherent. There is clearly a tradeoff between the path length in the anisotropic region and the strength of the anisotropy in that direction, hence in D″—where the layer thickness determines the path length—our knowledge of δV_{S} in any particular direction is limited by the uncertainty in exactly where in the lowermost mantle the anisotropy lies.

The elasticity tensor can be visualised by examining V_{P} and V_{S} as a function of direction. We present the elastic behaviour of materials using upper hemisphere diagrams, explained in Figure 3. For all directions, we calculate the phase velocities as described above and show V_{P} and δV_{S} with colour. Additionally, the orientation of the fast shear wave, S_1, is shown by black ticks. In these diagrams, we show the variation in elastic properties with respect to the three cartesian axes, 1, 2 and 3. Figure 3 shows the elastic constants for a set of mantle peridotites taken from Mainprice and Silver (1993). The 1–2 plane corresponds to the foliation in the sample, which probably results from a shear fabric. The 1-direction is aligned with the lineation, which probably shows the shear direction.

2. Measuring seismic anisotropy

The measurement of seismic anisotropy in the Earth has become routine for a limited number of techniques. In the deep mantle, work has mostly been directed towards observing the primary, unambiguous product of the presence of anisotropy: shear wave splitting in phases which traverse the D″ region. However new approaches are becoming available which can directly invert for anisotropic structure within the lowermost mantle using a broader range of data. Previous reviews of observations of D″ anisotropy are in Lay et al. (1998), Kendall (2000), Moore et al. (2004) and Wookey and Kendall (2007)

2.1. Correcting for the upper mantle

Measuring anisotropy in the deepest part of the mantle is not straightforward, as the upper mantle is known to be widely anisotropic itself (for a review, see Savage, 1999). The most common means of accounting for the effect of upper mantle anisotropy on D″-traversing phases is to use a correction based on SKS splitting measurements. This phase traverses the outer core as a P wave and converts to a vertically polarised S wave (SV) at the CMB, hence is unsplit upon re-entering the lower mantle (Figure 4). Making the assumption of lower mantle isotropy, SKS should only split when encountering D″ and the upper mantle.

SKS studies are now numerous and successfully explain many features of upper mantle dynamics, on the basis that SKS's path length in D″ is relatively small because the phase travels nearly vertically, and anisotropy in the lowermost mantle should not affect splitting in SKS much. Niu and Perez (2004) and Restivo and Helffrich (2006) compared SKS and

SKKS phases globally to investigate whether the lowermost mantle has an effect on such phases. In some individual cases in regions of high shear velocity, such as beneath eastern Canada, some discrepancy between SKS and SKKS was seen, which the authors attribute to D″ anisotropy related to LPO of post-perovskite or some other non-VTI mechanism. Overall, however, they found no significant departure from a mechanism in which SKS is not split in D″. This implies one of three things: anisotropy is not strong in D″, which does not appear to be the case from other measurements; anisotropy in D″ is not strong enough to be noticeable for near-vertical rays like SKS-SKKS, which have a relatively short path there; or the style of anisotropy (*e.g.*, VTI) means that radially polarised rays are not split, as azimuthal anisotropy may cause splitting in SKS-SKKS phases (Hall et al., 2004). This presents a puzzle for future studies of lowermost mantle anisotropy, as shall be explored.

If we continue with the assumption that SKS splitting reflects only upper mantle anisotropy, then it can be used to remove the receiver-side splitting which occurs in a D″-traversing phase when reaching the seismometer. The ray paths in the upper mantle of S, ScS and Sdiff are close to that of SKS for the distances discussed here, and their Fresnel zones at periods of 10 s all overlap significantly down to $\sim$300 km, so the effect of heterogeneity beneath the receiver is addressed. This does not account for anisotropy beneath the earthquake, however. One approach to address this is to use very deep-focus events (*e.g.*, $>$500 km), which presumably do not experience much of the upper mantle anisotropic fabric as olivine is only stable down to $\sim$410 km. However, Wookey et al. (2005a), Rokosky et al. (2006) and Wookey and Kendall (2008), for instance, show that there is observable splitting beneath even some deep events ($<$600 km), so this assumption may increase uncertainties in observations of lowermost mantle splitting where no source-side corrections are made.

Further difficulties with SKS splitting-based corrections when examining lowermost mantle-traversing phases are that in order to adequately correct for anisotropy beneath the receiver, one must have a good knowledge of the type of anisotropy present there, as dipping or multiple layers of anisotropy will lead to observed splitting having a strong dependence of the incoming polarisation of S-ScS-Sdiff. Choosing recording stations with many SKS measurements from a wide range of backazimuths can help alleviate this. A 90° or 180° periodicity in the splitting parameters ϕ and δt compared to the backazimuth betray the presence of complex upper mantle anisotropy (Silver and Savage, 1994), which should be avoided. Equally, stations which show little or no splitting across all backazimuths may be used with no correction. For especially well studied regions, it may be possible to correct for even complicated types of anisotropy (Wookey and Kendall, 2008), but the ability to uniquely interpret such SKS splitting measurements is rare.

An additional factor to consider in using SKS measurements as an upper mantle correction is that S and SKS phases are of different slowness, so their incidence angles beneath the receiver differ by up to $\sim$20°, depending on the epicentral distances being investigated. In general, this will lead to a difference in the splitting accrued along the rays in the upper mantle, hence an SKS-derived correction may not be appropriate. However, for an assumed hexagonal anisotropy with a horizontal symmetry axis beneath the station, the difference is small, and it appears in many studies the correction is adequate. Figure 5 shows the receiver-side upper mantle splitting which occurs in SKS and S in a 250 km-thick anisotropic layer. The elastic constants are of those shown in Figure 3 (Mainprice and Silver, 1993) with an imposed hexagonal symmetry. For SKS in the distance range $90° \leqslant \Delta \leqslant 120°$ (typical for upper mantle SKS splitting studies), the range of incidence angles is small (10–6°), and consequently there is almost no variation of splitting parameters with backazimuth. For S in the distance range $60° \leqslant \Delta \leqslant 80°$, incidence angles are ∼23–18°, and splitting in S shows some small variation with backazimuth. However, because the style of anisotropy is relatively simple, the difference in splitting parameters between S and SKS is very small—the fast orientations ϕ are indistinguishable, and the delay times are less than 0.3 s different, which is similar to the typical error in δt.

2.2. SH-SV traveltime analysis

The most straightforward way to infer anisotropy in D″ is to compare the arrival times of the two components of a shear phase when polarised horizontally (SH) and vertically (SV) (or, respectively, the tangential and radial components), after correcting for upper mantle anisotropy. The phases studied are usually S, ScS and Sdiff, and the assumption is made that the wave travels approximately horizontally (CMB-parallel) when bottoming in D″. Therefore, if SH arrives first, one can infer that along this azimuth the velocity is faster in the tangential direction than the radial ($V_{\mathrm{SH}} > V_{\mathrm{SV}}$). Figure 6 gives an example of this method.

In any study, constraining the source of the anisotropy to D″ is the main difficulty. There is good reason to suggest that the lower mantle above D″ is isotropic (*e.g.,* Meade et al. 1995; Montagner and Kennett 1996; Panning and Romanowicz 2006), therefore taking pairs of phases—where one spends some time in D″ and the other avoids it—can be used to remove upper mantle effects. Figure 4 shows ray paths for the major phases used: S, ScS, and Sdiff.

Some of the earliest studies (*e.g.*, Lay and Young, 1991; Vinnik et al., 1995) inferred anisotropy by looking at the retardation (relative to SHdiff), amplitudes and phase shifts of SV waves diffracted along the CMB (SVdiff). However, anisotropy is not the only possible cause of these effects for waves diffracted past distances of $\Delta \gtrsim 95°$, as shown by Maupin (1994) and Komatitsch et al. (2010). They model shear wave propagation in isotropic Earth models using the Langer approximation with perturbation theory, and spectral element method respectively, to show the early onset of SHdiff relative to SVdiff because of SV's coupling with the outer core, hence caution is needed in ascribing anisotropy to D″ on the basis of measurements of Sdiff at large distances: detailed full-waveform modelling and accurate isotropic Earth models are needed.

The majority of observations comparing SH and SV traveltimes show $V_{\mathrm{SH}} > V_{\mathrm{SV}}$, with $0.5\% \leqslant \delta V_{\mathrm{S}} \leqslant 3\%$, particularly in higher-than-average V_{S} regions, such as beneath subduction zones. Table 1 and Figure 7 summarise the observations for regional measurements of splitting in D″. In general, however, it seems that around the Pacific rim, $V_{\mathrm{SH}} > V_{\mathrm{SV}}$. Beneath the central Pacific, the pattern is more variable: some studies find $V_{\mathrm{SH}} > V_{\mathrm{SV}}$, some $V_{\mathrm{SH}} < V_{\mathrm{SV}}$.

2.3. *Global inversion for anisotropy*

An extension of the above technique that can be made—in terms of searching for a VTI structure—is to produce a global inversion for a ratio of V_{SH} and V_{SV}; usually the parameter $\xi = V_{\mathrm{SH}}^2/V_{\mathrm{SV}}^2$ is sought. Whilst global 1–D models of V_{S} such as PREM (Dziewonski and Anderson, 1981) sometimes include radial anisotropy in the upper mantle, at greater depths the inversions are generally isotropic. Montagner and Kennett (1996) used normal mode and body wave data to infer that $\xi > 1$ (*i.e.*, $V_{\mathrm{SH}} > V_{\mathrm{SV}}$) in D$''$ on a global scale. This matches the majority of local observations of SH-SV traveltimes. Recently, Panning and Romanowicz (2004, 2006) have inverted a global dataset of long-period three-component S waveforms to obtain a 3–D model of V_{P}, V_{S}, source parameters and ξ throughout the entire mantle. Any such study will be prone to difficulties in correcting for the strongly anisotropic crust and upper mantle, however, so great care is necessary to ensure that this does not contaminate the resulting model (Lekic et al., 2010). Equally, such models will necessarily suffer from sampling bias associated with the location of earthquakes and seismometers because of potentially limited azimuthal coverage of D$''$. With observations along only one ray path, it is not possible to resolve whether VTI is a good approximation. However, the model agrees with regional observations, showing $V_{\mathrm{SH}} > V_{\mathrm{SV}}$ where V_{S} is higher than average, especially around the Pacific rim subduction zones. Where V_{S} is relatively low, such as beneath the central Pacific and beneath Africa, $V_{\mathrm{SV}} > V_{\mathrm{SH}}$. Similarly to the work of Montagner and Kennett (1996), it also predicts $\xi > 1$ for D$''$ on average (Figure 8). Kustowski et al. (2008) invert surface and body waves for 3–D anisotropic mantle velocities using similar data, but find strong tradeoffs in the lowermost mantle between V_{S} and ξ, and the anisotropic structure in D$''$ correlates poorly between the two models. It seems that at present there is still some room to improve on current global models.

2.4. *Regional full-waveform inversion*

An alternative to producing a global map of anisotropy is to conduct regional full-waveform inversion of seismic data from phases which traverse D$''$. However, current studies are limited to assuming VTI in the lowermost mantle for computational and theoretical convenience. Using Tonga–USA raypaths, Kawai and Geller (2010) employ a full-waveform inversion for ξ beneath the central Pacific and find that $\xi < 1$ in D$''$, though there is little sensitivity to structure below about 150 km above the CMB. This agrees with other studies along similar raypaths, with $\xi \approx 0.97$, which is at the lower end of the range of values found previously. Here, it was necessary to impose a discontinuity of arbitrary depth at the top of the model, and upper mantle anisotropy was not included, so this may have a large impact on the uncertainty.

2.5. *Waveform analysis*

Whilst relatively straightforward to implement, a weakness of any study which compares SH and SV waves is the assumption of VTI. Recently, efforts have been made to relax this constraint and infer more complex type of anisotropy.

An approach used by Garnero et al. (2004a) and Maupin et al. (2005) is regional forward waveform modelling of S–ScS waves beneath the Cocos plate and the Caribbean. They infer small deviations of a TI symmetry of $\leqslant 20°$ away from VTI as the raypaths move east to west across the region. Using an SH-SV traveltime approach, this would and does appear as $V_{\mathrm{SH}} > V_{\mathrm{SV}}$, though energy will appear on both radial and transverse components for both fast and slow arrivals.

2.6. Measurements of shear wave splitting

Another recent advance towards allowing more complex forms of anisotropy to be studied is to apply the measurement of both ϕ and δt by grid search over the splitting parameters (Fukao, 1984; Silver and Chan, 1991) to lower mantle-traversing shear phases (Figure 9). (This and other techniques such as the splitting intensity method (Chevrot, 2000; Vinnik et al., 1989) are summarised by Long (2009)). This allows one to determine a more general form of anisotropy, as the fast orientation is not limited to being either parallel or perpendicular to the CMB. In principle, with measurements along one azimuth, one can distinguish whether VTI is a possible mechanism for D″ anisotropy or not, two azimuths can define a TTI-type fabric, whilst three can define an orthorhombic symmetry of anisotropy.

One application of the measurement of shear wave splitting is to examine differential splitting between the S and ScS, usually investigated at epicentral distances $55° < \Delta < 82°$ (with details of the method given by Wookey et al. (2005a)). Here, ScS samples D″, S turns above it, and both phases share a very similar path in the upper mantle. Because the ScS phase is approximately horizontal for most of its travel in D″ at these distances, the ray frame fast orientation ϕ' (also ϕ^*) is used (Wookey et al., 2005a). This measures the angle away from the Earth radial direction (*i.e.*, vertical) when looking along the ray. Hence, for VTI with $V_{\mathrm{SH}} > V_{\mathrm{SV}}$, $\phi' = 90°$. If $\phi' \neq 90°$, then another mechanism such as TTI must be responsible.

Single-azimuth S–ScS studies beneath the northwest Pacific (Wookey et al., 2005a), Cocos plate Rokosky et al. (2006) and southeast Asia (Thomas et al., 2007) have been conducted. Beneath the Cocos plate and southeast Asia, whilst there is some variability, in general fast directions do not depart much from being horizontal. Wookey et al. (2005a), however, found that the fast orientations dipped southeast towards the central Pacific by about 45°, which is a significant departure within the stated error of 7°. Assuming a TTI fabric, this actually provides a lower limit to the dip of the plane of isotropy, so clearly VTI in this region cannot explain the observations.

Recently, studies using two azimuths of S–ScS paths have been conducted. Beneath northern Siberia, Wookey and Kendall (2008) find that for waves travelling north from Hindu Kush events to stations in Canada, $\phi' = 89°$ (the fast orientation is approximately horizontal in D″), whilst east-west paths from the Kuril arc to stations in Germany show $\phi' = 35°$ (the fast direction dips 55° to the south). Beneath the Caribbean and North America, Nowacki et al. (2010) examine three regions with uncertainties of $\leqslant 10°$ for all azimuths. For ray paths travelling north to stations in North America from events in South America, $\phi' \approx 90°$, within error, which agrees with previous single-azimuth observations (Kendall and Nangini, 1996; Garnero and Lay, 2003; Garnero et al., 2004a). However, ray paths which cross these are not compatible with VTI: paths travelling northeast from the East Pacific Rise show $\phi' = -42°$ (dipping to the southeast), whilst those travelling northwest from the Mid-Atlantic Ridge show $\phi' = 45°$ (dipping south). A third region off the coast of northwest USA shows two paths with fast orientations $\geqslant 10°$ different to horizontal.

In the cases outlined above, where $\phi' \approx 45°$, the traditional SH-SV traveltime method would not observe any effects of anisotropy (Wookey and Kendall, 2007) (Figure 10). Equally, cases where $0° < \phi' < 45°$ cannot be distinguished from simple VTI where $V_{\mathrm{SH}} > V_{\mathrm{SV}}$. Hence the importance of not only resolving the fast orientation, but also incorporating a large range of azimuths, is hard to understate if we wish to make inferences about the nature and origin of seismic anisotropy from analysis of shear waves. It seems that, in contrast to our previously simple idea of horizontal fast directions beneath subduction zones, and vertical ones beneath upwellings, the the picture is more complex. If VTI is not a good approximation to the type of anisotropy in D″, then multiple-azimuth studies must become the norm, otherwise we are at the mercy of the specific, single event-receiver geometry as to whether we can resolve the true effect of CMB dynamics. At the same time, however, the Earth does not give up its secrets easily, as the location of landmasses and large earthquakes poses limitations on which regions of the lowermost mantle we can probe at present.

Given that several studies have now implied that D″ does not everywhere show VTI-type behaviour, it is prudent to assess the discrepancy between this knowledge and the conclusions of Niu and Perez (2004) and Restivo and Helffrich (2006) (Section 2.1). Because azimuthal anisotropy appears to be present beneath at least Siberia, the Caribbean, western USA, the eastern and northwest Pacific and southern Africa, we should expect that studies comparing SKS and SKKS should exhibit differential splitting between the two phases which emerge from the outer core in these regions. In fact, as pointed out, Long (2009) and Wang and Wen (2007) do observe this in regional studies. In addition, Restivo and Helffrich (2006), for example, also show strong anomalous splitting between the two phases beneath western USA and the eastern Pacific, whilst southern Africa is poorly sampled because of event-receiver geometries. Furthermore, the Caribbean is not well covered: anomalous splitting in SKS-SKKS is evident there also, even if the global trend does not show significant departure from VTI for the whole dataset. Another factor is that because SKS and SKKS are polarised vertically upon exiting the outer core, they will not be split by TTI where the dip direction is closely parallel or anti-parallel to the wave propagation direction. Perhaps the largest difference is that even SKKS at $\Delta = 110°$ spends around 350 km in a 250 km-thick D″ with $\langle V_{\mathrm{S}} \rangle = 7.3$ km s^{-1}, whereas ScS at 70° has a path over 1000 km. It may therefore be not so surprising that SKS-SKKS differential splitting is hard to observe. However, the small number of cases where it is seen (5 % of observations by Restivo and Helffrich (2006)) requires a good explanation that is still lacking.

3. Chemistry and mineralogy of the lower mantle

The properties of the lowermost mantle are of course determined by the bulk composition and which phases are stable at the pressures and temperatures there. In order to interpret seismic observations using geodynamic inferences, we must understand the single- and polycrystal behaviour of the solid phases present, and the possibility of the presence of melt. There are a number of steps which are necessary to use mineral physics data to predict flow from anisotropy. Firstly, which phases are present must be established. Then, single-crystal elastic properties and deformation mechanisms must be evaluated. These can then be used to determine polycrystalline behaviour in deformation, which can allow an aggregate anisotropic fabric to be predicted on the basis of a given deformation history. Often it is hard to separate these in experiments, for instance, which involve many crystals, and authors attempt to find single-crystal properties from polycrystalline measurements. However successful modelling of texturing and hence anisotropy requires knowledge of all of these properties.

Lowermost mantle mineralogy can be investigated with mineral physics experiments at CMB pressures and temperatures using apparatuses such as the laser-heated diamond anvil cell (LHDAC), but there are of course limitations. An important source of error in experiments is the pressure scales used (the Au scale of Tsuchiya (2003), versus the MgO standard of Speziale et al. (2001), amongst others). This means the stated pressure, and hence depth, of the transition from pv to ppv in experiments can range by as much as ± 10 GPa (± 200 km in the lower mantle) depending on the scale, which is an ongoing problem (Hirose, 2007). Another significant source of error comes from the high thermal gradients created in the cell by focussed laser heating and diamond's excellent thermal conduction.

Numerical calculations of the properties of materials at high pressure and temperature are another important technique. As for physical experiments, however, uncertainties are present, due to the approximations necessary in performing the calculations. Density functional theory (DFT; Kohn and Sham, 1965) provides the basis for most of the studies we mention, which determines material properties by solving Schrödinger's wave equation. DFT gives an exact solution to the problem, but relies on an unknown term (the exchange-correlation energy). Different approximations to this term lead to different biases in the calculations. For a review, see Perdew and Ruzsinszky (2010).

3.1. Composition and D″ mineralogy

The Earth's mantle is generally believed to be pyrolitic in composition (Ringwood, 1962; McDonough and Sun, 1995). This chemistry determines which mineral phases are present under the conditions of the lowermost mantle, though some experimental evidence suggests that a representative pyrolitic material, the KLB-1 peridotite, may not alone be able to reproduce the seismically-observed density in the lower mantle (Ricolleau et al., 2009). Input of other material such as mid-ocean ridge basalt (MORB) from subducting slabs must therefore play a role.

The phases present above D″ in a pyrolite composition are orthorhombic $MgSiO_3$ perovskite, with the likely incorporation of some Fe and Al (pv; Figure 11), cubic (Mg,Fe)O (ferropericlase, fpc) and $CaSiO_3$-perovskite (Ca-pv). Experiments suggest they are in the proportions 75, 20 and 5 % respectively (Kesson et al., 1998; Murakami et al., 2005) (Figure 12). For MORB, which is much richer in Al and Si, experiments show a very different mineralogy (Hirose et al., 1999; Ono et al., 2001; Hirose et al., 2005), with about 40 % pv, no fpc and 20 % Ca-pv. Significant amounts of a Na- and Al-rich phase, and a silica phase ($\sim$20 % each) are present.

In 2004, several authors discovered another phase transition in $MgSiO_3$ to the orthorhombic $CaIrO_3$ structure at about 125 GPa (around 2700 km depth) and 2500 K (Murakami et al., 2004; Oganov and Ono, 2004). The post-perovskite phase (ppv) has a structure of layers of SiO_6 octahedra parallel to (010), intercalated with layers of Mg ions (Figure 11, right).

Recently, studies have been carried out on pyrolite and MORB samples up to CMB conditions. In pyrolite, Murakami et al. (2005) observe the pv–ppv transition at ∼113 GPa (equivalent to ∼2500 km) and 2500 K, where the phase assemblage is ppv (72 %), fpc (21 %) and tetragonal or cubic Ca-pv (7 %). In MORB compositions, Ono and Oganov (2005) investigated pressures up to 143 GPa (Au standard) and temperatures of 3000 K. They observed ppv, Ca-pv, α-PbO_2-type (also called columbite) silica and a $CaTi_2O_4$-type aluminous phase. Ohta et al. (2008) also investigated MORB samples with similar results, except they found a Ca-ferrite ($CaFe_2O_4$)-type aluminous phase at lowermost mantle conditions. They suggest a transition in silica from the $CaCl_2$ to α-PbO_2 structure at around 115 GPa and 2000 K. Figure 12 summarises our current understanding of the phase proportions in the lower mantle.

Whilst we do not focus in this review on the gross variability of the phase assemblage at D″ conditions because of compositional changes other than pyrolite versus MORB, it is obviously important in the behaviour of the lowermost mantle, and there is increasing evidence that chemical heterogeneity must play a part in creating the seismic variability observed in D″ (*e.g.*, Simmons et al., 2009).

3.1.1. Pv–ppv phase boundary

How much pv or ppv is present in the lowermost mantle is still unresolved. For pure $MgSiO_3$, the phase boundary of course sharp and occurs at ∼110–120 GPa, or 2400–2600 km, hence D″ would be mainly composed of ppv. However with realistic amounts of Fe and Al, the phase boundary will be spread out over a range of pressures. Whether the region of costability is extended upward in the Earth by the addition of Fe and Al, or downwards, depends on the partition coefficient of the element between the two phases. If Fe, for instance, partitions more favourably into pv, then it will be stabilised down into the ppv stability field, and costability of the two phases will occur to greater depths than for the pure Mg endmember. Partitioning into ppv would conversely increase the mixed phase region upwards into pv's stability field. Thus this controls the amount of pv and ppv which are present in D″. Additionally, Fe^{2+} and Fe^{3+} will behave differently, and how much iron is ferrous (Fe^{2+}) depends on the oxidation state of the lowermost mantle. It might also be that if another phase like fpc is present into which Fe (or Al) partitions preferentially over pv and ppv, then this will buffer the Fe content and decrease the width of the two-phase region.

Pv and ppv do include Fe and Al in their structure in a pyrolitic composition (Murakami et al., 2005), so the phase boundary between pv and ppv in various compositions is important. Whilst progress is being made, there has yet to emerge a consensus on the partitioning of Fe in particular between fpc and ppv, versus fpc and pv, hence there remains uncertainty in the pressure range across which pv and ppv are both stable. It seems that the partition coefficient of Fe between pv and ppv, $K_{\mathrm{Fe}}^{\mathrm{pv/ppv}}$, is strongly dependent on Fe and Al content of the phases. Recent work at CMB conditions suggests $K_{\mathrm{Fe}}^{\mathrm{pv/ppv}} \approx 4$ (see Andrault et al., 2010, and their introduction for a recent concise review), and the phase boundary is predicted to be about 15 GPa or 300 km thick. Catalli et al. (2009) measure the transition width to be about 20 GPa (∼400 km) in a synthesised sample of $(\mathrm{Mg}_{0.9}\mathrm{Fe}_{0.1})(\mathrm{Al}_{0.1}\mathrm{Si}_{0.9})\mathrm{O}_3$, and less than that in a sample without Al ($(\mathrm{Mg}_{0.91}\mathrm{Fe}_{0.09})\mathrm{SiO}_3$), though this of course does not include the buffering effects of any other phases which are present in the Earth. Both studies suggest costability begins at pressures equivalent to 400–600 km above the CMB.

Sinmyo et al.'s 2008 study highlights the uncertainties in the measurements of K_{D}, finding that the large temperature gradient in the sample may cause the variability between studies. Further, uncertainties in the pressure scales mean it is hard to define at exactly what depth the beginning of the mixed-phase region starts. Notably, actual peridotite samples (Murakami et al., 2005) apparently contain ppv at D″ conditions.

An additional factor to consider is that the phase proportion curve may not be linear across the transition, so larger or smaller amounts of ppv may be present than expected for a given pressure. One attempt to quantify this (Hernlund, 2010) suggests ppv is likely to exist in significant proportions (>50 % of the mantle) after just a few tens of kilometres of the transition.

Measurements of the Clapeyron slope of the pv–ppv show it likely lies in the range 7–14 $\mathrm{MPa\,K^{-1}}$ (Oganov and Ono, 2004; Tsuchiya et al., 2004; Ono and Oganov, 2005; Hirose et al., 2006; Tateno at al., 2009). This positive value implies that colder areas of the lowermost mantle will be enriched in ppv relative to hotter ones, and also offers the possibility that because of the steep geotherm near the CMB, so-called 'double-crossings' of the phase boundary might occur, leading to lenses of ppv-rich mantle bounded above and below by pv-rich areas (Hernlund et al., 2005; Wookey et al., 2005b). The effect this might have on the development of anisotropy from LPO of ppv is intriguing but poorly understood at present.

3.2. Single-crystal elasticity of D″ minerals

With knowledge of the approximate proportions of phases present in the lowermost mantle, an understanding of the individual minerals' properties and relative stabilities is necessary to make predictions about the behaviour of seismic waves passing through this region. Hence there has been much interest in using both experimental and theoretical methods to investigate these properties. Recent reviews of some of the work done on lowermost mantle phases—mainly pv, ppv and fpc—can be found in Hirose (2007), Shim (2008), Ohtani and Sakai (2008) and Trønnes (2010), amongst others. Here we discuss the most basic property of the phases in D″ for our purposes, their elasticity, which provides a first-order idea of their contribution to seismic anisotropy.

3.2.1. Perovskite

Magnesium silicate perovskite (with about 10 % Fe and a few percent Al in the structure) is the most abundant mineral phase in the Earth, and is likely present in some portions of the bottom few hundred kilometres of the mantle. Because pv and ppv make up most of the lower mantle, they are the primary phases to affect seismic waves, and thus most important to understand well. Although perfect perovskites are cubic, pv is orthorhombic due to the rotation of the SiO_6 octahedra (Figure 11, left).

Single-crystal elastic constants for pv at lowermost mantle conditions are shown in Figure 13. Elastic constants for pv have been calculated by Oganov et al. (2001), Wentzcovitch et al. (2004), Wookey et al. (2005b) and Wentzcovitch et al. (2006) at CMB pressure, the latter two at high T. Figure 13 shows that there is some discrepancy between the calculations, which appears to be due to differences in the C_{12}, C_{22} and C_{33} terms. The maximum δV_S is between about 13–20 %, which is moderately but not very strongly anisotropic.

3.2.2. Post-perovskite

With the discovery of ppv (Iitaka et al., 2004; Murakami et al., 2004; Oganov and Ono, 2004; Tsuchiya et al., 2004), there has been an understandable focus on its elasticity, phase stability, and so on, as explanations of lowermost mantle observations.

Intuitively, the orthorhombic ppv structure should be more seismically anisotropic than pv due to the layering of the SiO_6 octahedra, and this appears to be the case: the b-axis is more compressible than the a- and c-axes (Guignot et al., 2007; Mao et al., 2010). Elastic constants at D″ P and T have been calculated from experiments for ppv (Mao et al., 2010); *ab initio* calculations have recently been made by Wookey et al. (2005b), Stackhouse et al. (2005b) and Wentzcovitch et al. (2006).

Figure 14 shows the elastic anisotropy for ppv at high temperature, comparing the theoretical calculations ($MgSiO_3$) at 4000 K to those of Mao et al. (2010) ($(Mg_{0.6}Fe_{0.4})SiO_3$) at 2000 K. It is clear that there is some variation between the calculations. The experimentally-derived results show the largest δV_S, with $\delta V_S = 42\,\%$ along [010]. Otherwise, the pattern is quite similar between the studies of Stackhouse et al. (2005b) and Mao et al. (2010), despite the difference in Mg#. This agrees with the analysis of Wookey and Kendall (2007), who suggest from combining *ab initio* elastic constants for the $MgSiO_3$, $FeSiO_3$ (Stackhouse et al., 2006) and $AlSiO_3$ (Stackhouse et al., 2005a) ppv endmembers in pyrolitic proportions that they do not differ significantly from those of pure Mg case. The general pattern of anisotropy differs slightly when considering the constants of Wentzcovitch et al. (2006), mainly due to differences in C_{11}, C_{33} and C_{13}; the reason for this discrepancy is still unclear and hopefully future work will better constrain our knowledge of the single-crystal elasticity of ppv. It is notable that theoretical calculations with realistic amounts of Fe and Al in Mg-pv and -ppv are difficult because the number of atoms in the simulations becomes large, hence the effect of their incorporation is uncertain.

3.2.3. Ferropericlase

As the second most abundant mineral phase in the lowermost mantle, fpc is an important control on the behaviour of seismic waves in D″. Assuming a pyrolitic mantle, an approximate Mg# of 0.9 with Fe# = 0.1 is the likely composition. (Mg,Fe)O is stable throughout the lower mantle, though much recent interest has been shown in a possible change of its properties due to the change in the spin state in Fe which may occur at midmantle pressure and temperatures. We do not discuss in detail the spin transition in fpc further as it appears this occurs higher in the mantle than D″ (∼2200 km; *e.g.*, Komabayashi et al., 2010); of relevance is that Fe in fpc is likely in the low-spin state in the lowermost mantle. (For a recent review of the spin transition in fpc, see Lin and Tsuchiya, 2008.)

Because fpc is cubic, the three constants required to describe the elastic behaviour of the structure are C_{11}, C_{12} and C_{44}. Single-crystal elastic constants for fpc $(Mg_{0.9}Fe_{0.1})O$ have recently been determined from experiment by Marquardt et al. (2009) up to 81 GPa (∼1900 km) at ambient temperatures. Karki et al. (1999) calculate the elastic constants up to 150 GPa (greater than mantle depths) and 3000 K using *ab initio* methods for the pure Mg endmember, whilst Koci et al. (2007) perform calculations at 0 K up to 150 GPa for a range of Fe proportions up to 25 % $((Mg_{0.75}Fe_{0.25})O)$. Figure 15 shows a selection of single-crystal elastic constants for MgO from theoretical calculations and $(Mg_0 0.9Fe_{0.1})O$

It appears that the main effect of Fe in fpc is to decrease C_{11} and C_{44}, and increase C_{12} (Figure 15; Koci et al., 2007), which in general will decrease the anisotropy of the crystal (C_{12} becomes closer to $(C_{11} - 2\,C_{44})$, as for the isotropic case). Little work has been conducted with Fe in the structure at high pressure, however, so these results are for high- or intermediate-spin states of Fe, and it is not clear what effect low-spin Fe might have on the anisotropy of fpc. As with pv and ppv, a large unknown at present is the partition coefficient between these phases, hence our knowledge of the likely Fe content of any of them at a particular pressure and temperature is limited.

3.2.4. Other phases

Whilst pv–ppv and fpc are the dominant phases in a pyrolitic composition at D″ conditions, Ca-pv along with silica and aluminous phases are present in much larger proportions in a MORB composition, hence knowledge of these phases is still important.

Ca-pv is predicted to undergo a transition from cubic to tetragonal due to rotation of the SiO_6 octahedra at around 2000–2500 K at the CMB on the basis of *ab initio* molecular dynamics (MD) simulations (Adams and Oganov, 2006; Stixrude et al., 2007), so potentially in cold regions of the mantle this lower symmetry phase may exist. In contrast, Li et al. (2006b) suggest—also from MD—that the tetragonal phase is stable throughout the lower mantle. However, experiments at both pressures and temperatures of the lowermost mantle have yet to be conducted, so the phase diagram of Ca-pv is uncertain. Li et al. (2006a), Adams and Oganov (2006) and Stixrude et al. (2007) report elastic constants for Ca-pv at CMB conditions. Cubic Ca-pv appears to be moderately anisotropic, showing maximum δV_S of ∼20 %, comparable to ppv and fpc, however the fact that it is a minor constituent of the lowermost mantle means it is often neglected as a possible contributor to seismic anisotropy.

The silica phases most likely present in D″ are in the orthorhombic $CaCl_2$ or α-PbO_2 (also called columbite) forms, with the transition occurring at about 110–120 GPa (2500–2600 km). The implications for the presence of mainly the α-PbO_2-type in D″ are not clear, as there are as yet no measurements of velocities or elastic constants for it at lowermost mantle temperatures and pressures. Karki et al. (1997a) do report constants at high pressure and 0 K from *ab initio* calculations (based on structure parameters reported in Karki et al. (1997b)). At least at 0 K, the α-PbO_2-type silica shows a maximum δV_S of ∼15 %, so appears unlikely to be a major candidate anisotropic phase in D″, given its low abundance. Future high-T work to elucidate the properties of free silica in the lowermost mantle will have important repercussions for models where subducted MORB at the CMB plays a large role in seismic anisotropy.

3.3. Lattice preferred orientation and slip systems in D″ phases

In order to generate anisotropy, individual anisotropic crystals must be aligned over large lengthscales in a lattice- (or crystal-) preferred orientation (LPO, or CPO) (Figure 16A). Assuming that the phase undergoes deformation which is accommodated by slip on a crystallographic plane (such as dislocation glide), the relative strengths of the slip systems active in the crystal determine how the mineral aligns. Furthermore, how an aggregate of individual crystals deforms depends on the phases present and their orientations.

At present, our understanding of slip systems and aggregate texture development for mono- and polymineralic assemblages of phases at CMB conditions is poor, mainly because it is currently impossible to recreate mantle temperatures, pressure (both very large) and strain rates (very low) on large polycrystalline samples in the laboratory. However, various experimental and theoretical methods have been used to examine the likely deformation mechanisms.

There are two main approaches to evaluating the LPO caused by deformation in mantle minerals. Firstly, one can investigate the phases at D″ conditions in the LHDAC, compressing the sample by increasing the confining pressure during the course of the experiment, leading to uniaxial deformation in the cell. Typically, radial X-ray diffraction data are taken and the intensity of the individual diffraction lines is taken to correspond to the number of crystals which are aligned in the orientation appropriate to cause the diffraction. The ellipticity of the diffraction rings is a measure of the differential stress within the sample. Thus a pole figure (orientation distribution function, ODF) can be calculated for the crystallographic directions and a dominant slip system inferred. There are a number of limitations to this technique, however—primarily, the sample size is very small (a few μm^3), hence the amount of shortening is limited, and the sample is rarely actually at D″ temperatures when observations are made: it is usually heated beforehand for some time, but is cooling when lattice parameters are measured.

Alternatively, one can look at structural analogues of lowermost mantle phases which are stable at conditions more easily achieved in the laboratory. Hence larger samples ($\sim$20 mm^3) can be compressed, and the texture created examined directly. $CaIrO_3$, $MgGeO_3$ and $MnGeO_3$ have been used in this way, for instance, to investigate the slip system in ppv as they share the same structure. So far, the Kawai and D-DIA (differential-DIA) apparatuses have been used to compress samples with a shear plane imposed at an angle to the compression direction. (For a review of terminology and methods, see Durham et al. (2002).) The sample is typically sheared to a shear strain of $\gamma \sim \mathcal{O}(1)$, and the sample recovered and analysed with electron backscatter diffraction (EBSD) to determine the crystallographic orientation of potentially thousands of crystals. An ODF can be calculated, and slip systems inferred. Note that in such experiments, complex behaviour of polycrystalline material can be investigated, and several slip systems may operate. It is also notable that the presence of other phases as compared to a single-phase assemblage can change the deformation behaviour of an aggregate. This means that our long-term understanding of how material deforms in D$''$ must rely on calculations or experiments on likely lowermost mantle compositions.

Theoretical methods are also used to investigate deformation mechanisms, typically using the generalised stacking fault (GSF) within a Peierls-Nabarro dislocation model. Often, *ab inito* methods are used to find the GSF energy, feeding the Peierls-Nabarro model. Walker et al. (2010) summarise the main techniques used. Others, such as Oganov et al. (2005), use metadynamics to find new structures by perturbing the structure being studied, and allowing it to relax to another, effectively pushing the structure over an energy barrier to a new arrangement.

The purpose for this review of understanding single-crystal deformation mechanisms is that we require such knowledge in order to infer deformation from measurements of seismic anisotropy. With values for the relative strengths of slip systems, one can predict the aggregate ODF and subsequent anisotropy of a polycrystalline assemblage. The predicted slip systems may be used, for example, in a viscoplastic self-consistent model (Lebensohn and Tomé, 1993; Wenk et al., 1991) and subjected to a known strain history, resulting in predictions which can be compared to observations.

3.3.1. Perovskite

For pv, theoretical calculations have been combined with experiment to determine the relative strengths of the dominant slip systems by Mainprice et al. (2008). Using a Peierls-Nabarro dislocation model, they infer that the [010](100) system is easiest at lowermost mantle conditions. This agrees qualitatively with experiments performed at lower pressures than present at the CMB (Cordier et al., 2004; Merkel et al., 2003), though high-temperature studies are still awaited. Even with 100 % alignment of the phase, the maximum δV_S is $\sim$2 %, which is significantly less than is the case for ppv or fpc. Hence it seems that, compared to fpc and ppv, pv is a poor candidate phase to explain the near-ubiquitous observation of D$''$ anisotropy.

3.3.2. Post-perovskite

Table 2 summarises the experimental studies to date on slip systems in ppv and its structural analogues. It is clear that little consensus exists regarding the dominant slip system, with slip on (100), (010), (001) and {110} all suggested by at least one study. However, there is agreement for the slip system in $CaIrO_3$. Recent DAC and large-volume deformation experiments seem to confirm (010) as the likely slip plane for relatively large strains, with perhaps [100] the slip direction. Most studies also detect a different texturing associated with the transformation from the pv to ppv structure—a so-called 'transformation texture'—consistent with slip on $\langle\bar{1}10\rangle\{110\}$ (Walte et al., 2009; Okada et al., 2010; Hirose et al., 2010). However, whether $CaIrO_3$ is a 'good' analogue for ppv—in the sense that it deforms in the same way—is under debate (Walte et al., 2009; Hirose et al., 2010; Miyagi et al., 2010; Mao et al., 2010; Okada et al., 2010). Hence whilst the advantages of using relatively large, polycrystalline samples are obvious, care is needed in directly applying the results of analogues to the case of the lowermost mantle.

Earliest theoretical work suggested on the basis of structural arguments that slip on (010) should be easiest, as this is the plane in which the SiO_6 octahedra lie, and indeed this agrees with experiments on $CaIrO_3$. Carrez et al. (2007) suggest the system [100](010) on the basis of Peierls-Nabarro modelling. Metsue et al. (2009) also find the same, though point out that despite the similarity between the predicted slip systems in ppv and $CaIrO_3$, the starting single-crystal properties for the two phases are quite different, so drawing conclusions from such bases is difficult.

The observed 'transformation texture' of slip on $\{110\}$ (*e.g.*, Walte et al., 2009; Okada et al., 2010) adds complexity to our picture of the relation of deformation to anisotropy. If it is replicated in the pv–ppv transition, then it may be that descending mantle will acquire a certain texture for a time, which changes as strain increases. Hence future work to pin down whether such a process occurs in the Earth is important.

3.3.3. Ferropericlase

As the reader might have come to expect, great difficulties in experiments and theoretical calculations at extreme conditions mean there is disagreement between authors regarding the likely slip system in fpc. For NaCl-type cubic crystals, slip along $\langle 110\rangle$ is expected to dominate, hence one might expect $\{110\}$ to be the likely slip planes for fpc (Karato, 1998). However, other slip planes may also be dominant, and high temperatures will affect the activation energies of the slip planes. *Ab initio* calculations for MgO and Peierls-Nabarro modelling (Carrez et al., 2009) suggests that the active slip system at low temperature is $\frac{1}{2}\langle 110\rangle\{110\}$, though the $\frac{1}{2}\langle 110\rangle\{100\}$ system becomes relatively easier with increasing pressure.

Experiments on the pure-Mg endmember at 47 GPa and ambient temperature by Merkel et al. (2002) in the LHDAC suggest slip on $\{110\}$. Contrasting results were found by Long et al. (2006), who used a large-volume press to deform a sample at 300 MPa and ∼1400 K for a range of compositions ($0 \leqslant \mathrm{Mg\#} \leqslant 1$). For pure MgO, [001] tends to align with the shear direction, whilst [110] aligns for FeO. Even for $\gamma \approx 4$, though, the development of LPO was fairly weak.

Yamazaki and Karato (2002) used compositions of $\mathrm{Mg\#} = 0.25$ and 1.0 at $P = 300$ MPa, $T \approx 1000$ K with a very similar experimental setup to that of Long et al. (2006). They find slip on $\{100\}$ or $\{111\}$ is likely.

Whilst knowledge of individual slip systems is important, in the long term we require experiments and calculations on polycrystalline, multi-phase assemblages of the kind we expect to exist at D″, as experience suggests monomineralic assemblages at vastly different conditions are not necessarily accurate proxies for the real thing. An improvement would be knowledge of the relative strengths of the several slip systems operating in the single crystal of any given phase. This would then allow one to calculate the development of texture under a known strain. An issue which seems very difficult to resolve experimentally is the vast difference in strain rates between studies and the Earth. It seems likely that strain rates in the deep mantle are $\dot{\epsilon} \approx \mathcal{O}(10^{-16})$–$\mathcal{O}(10^{-14})$ s^{-1}, whilst at present we achieve $\dot{\epsilon} \gtrsim 10^{-4}$ s^{-1}, so whether we can ever recreate such strains is a hard question to answer positively.

4. Shape-preferred orientation

Thus far we have only considered the LPO of mineral phases as a potential cause of lower mantle anisotropy. An entirely separate cause of anisotropy is the sub-wavelength layering or ordering of material with contrasting elastic properties (Figure 16B and 16C). The anisotropy may be due to the periodic layering of different materials or the preferred alignment of inclusions like melt pockets.

If SPO is the cause of lowermost mantle anisotropy, it may still be a result of deformation processes. To infer the link between deformation and observed anisotropy we must appeal to effective medium theories that predict the anisotropy. A number of approaches exist, but they can be divided into those that assume constant strain (*e.g.*, Hudson, 1980b) or those that assume constant stress (*e.g.*, Tandon and Weng, 1984; Sayers, 1992). A further complication involves the degree of interconnectivity between fluid inclusions, which leads to frequency dependent anisotropy (for a review see Hall and Kendall, 2001). Assuming an effective medium theory, an aggregate elastic tensor can be constructed and then used to predict the seismic observables along a given ray path. Holtzman and Kendall (2010) describe such an approach for linking a number of anisotropy mechanisms to strain partitioning at plate boundaries.

Spheroidal inclusions lead to a hexagonal symmetry or TTI (see examples in Figure 16B and 16C). A more complex orthorhombic medium results if the inclusions are scalene ellipsoids (three axes of different lengths). However, on the basis of natural samples, which tend to contain either elongate (prolate spheroidal) or flat (oblate spheroidal) inclusions, it seems that in most settings one axis will be significantly different from the other two. An example of each are L- and S-tectonites in subduction settings (Tikoff and Fossen, 1999).

With respect to the lower mantle, Kendall and Silver (1996; 1998), for example, model the effects of spheroidal inclusions of contrasting velocity. They show that small volume-fractions of oblate or disk-shaped inclusions of melt are highly efficient in generating seismic anisotropy. In order for periodic layering or aligned inclusions to produce an effective anisotropy, and not simply heterogeneity, the wavelength of the layering must be less than the dominant seismic wavelength. Indeed a way of discriminating between LPO and SPO anisotropy may be through observations of frequency dependent effects. For example, small-scale heterogeneity may scatter high-frequency seismic energy, but such a medium may be effectively anisotropic to long wavelength energy (Rümpker et al., 1999).

Also compatible with observations might be the complementary presence of both SPO and LPO. If, for instance, strain partitions into one weaker phase in a multi-phase mixture (*e.g.*, a solid and liquid, or two solid phases with contrasting strengths; *e.g.*, Ammann et al., 2010), then we might expect shear bands to form, as is frequently observed in surface geology. If the bands are of the appropriate length scale, they might have an SPO contribution to seismic anisotropy, whilst the highly deforming material in the bands—or even outside, for the case of melt-rich bands—may still deform to produce LPO. Hence the division between LPO and SPO is not necessarily clear whilst our knowledge of the lowermost mantle is at this limited stage.

A major unknown in this sort of analysis is that the plausibility of melt in the lowermost mantle is still speculative. Furthermore, much work is needed to better establish the material properties of such melt, be they primordial in origin, the remains of subducted palaeo-oceanic crust (basalt) or material derived from the outer core.

5. Geodynamics

While knowledge of the deformation mechanism of lowermost mantle materials is limited (see section 3.3), one approach to assessing how likely they are to be realistic is to consider the first-order flow exptected just above the CMB. Topography on the CMB is limited to a few kilometres at most (*e.g.*, Tanaka, 2010), and the outer core is liquid with a free-slip surface above, so it seems highly likely that flow just above the CMB is mainly horizontal. If we assume this, we might be able to mark as unlikely some of the proposed deformation mechanisms for ppv, and then use the remainder to suggest slightly more nuanced flow situations in D″. We explore this further in section 6.

Global models of mantle flow have matured rapidly with increasing computer power and new techniques over recent years, and inferring the first-order flow field at the CMB by including geophysical observables such as recent plate motions and likely phase stabilities and rheologies is now possible. Alongside this, models of mantle flow have developed which are derived from seismic tomography, with the constraints of mineral physics, geoid and plate motion data.

Where there is good evidence from seismic wave speed tomography (*e.g.*, Ritsema et al., 1999; Montelli et al., 2004) of subducting slabs reaching the lowermost mantle, such as the Farallon slab beneath North America, we can make slightly more detailed inferences regarding the likely large-scale flow field. A simple approach used frequently (*e.g.*, Wookey and Kendall, 2007; Yamazaki and Karato, 2007; Miyagi et al., 2010) is to assume horizontal flow occurs at the CMB, and hence slip systems which produce fast orientations within the slip plane are the likeliest to match the majority of observations which suggest $V_{\mathrm{SH}} > V_{\mathrm{SV}}$ in D″. As section 2.6 shows, however, requiring horizontal fast directions in all directions does not match with observations, so such assumptions must be revisited.

One constraint on the kind of deformation experienced in such a situation is to construct models of mantle flow with an imposed subduction of a thermally negatively buoyant slab. McNamara et al. (2003), for example, use a general 2D cylindrical model with diffusion and dislocation creep to search the parameter space of variables such as slab thickness and strength, and relative activation energies of the two creep regimes. They find that dislocation creep dominates around the slab, and at the base of the mantle beneath the slab, whilst the rest of the mantle is likely deforming in diffusion creep, hence not producing significant LPO. They also claim that LPO in such a model requires $\gamma \gtrsim 4$ to develop. With this method, where the whole Earth's mantle is modelled, but without imposing the constraints of observed plate motions, the results can be qualitatively, and to some extent quantitatively compared to deformation mechanisms in lowermost mantle mineral phases.

In order to construct models which are useful in understanding how the mantle flows in D″, a huge number of parameters are necessary, only some of which are known well. One-dimensional radial viscosity profiles (*e.g.*, Mitrovica and Forte, 2004), for instance, place a strong control on the depth and extent of subduction, which would then affect the flow field above the CMB. Although these are constrained from present-day observables (mainly isostatic glacial rebound of the surface for shallow depths, and mineral physics data much deeper), obviously there is likely to be lateral variations in viscosity as well—such as that introduced by a cold slab—which can only be modelled with accurate understanding of the effect on viscosity of temperature, composition, mineralogy, and so forth. Other large unknowns are the temperature at the CMB and the effect of composition and temperature on the density of mantle phases.

In some studies (*e.g.*, Wenk et al., 2006; Merkel et al., 2006, 2007), workers take 'general' models of flow of this kind and test for the type of anisotropy produced by a given deformation mechanism when traced through the flow field. Assuming a certain flow field as suggested by the convection model, they trace particles through the field and apply a viscoplastic self-consistent (VPSC) model (*e.g.*, Lebensohn and Tomé, 1993, Wenk et al., 1991) to calculate the texture developed for a polycrystalline aggregate using a set of slip system activities relevant to the phases being tested. The resulting aggregate elastic tensor is constructed from the single crystal constants and the orientation distribution function (ODF) of the phases in the aggregate, and can then be compared with seismic observations from similar settings—that is, beneath subducting slabs.

Another approach to modelling flow in the mantle is to seek a 'true' picture of what is happening at present. Using seismic travel time picks, plate motion reconstructions (Lithgow-Bertelloni and Richards, 1998), gravity measurements, dynamic topography and other constraints, various authors (*e.g.*, Tackley, 2000; Trampert et al., 2004; Simmons et al., 2009) have attempted to invert for the present-day or recent flow field in the mantle. Much of this work depends on the particular relationship between seismic wave speed and density in order to asses whether only thermal, or thermal and compositional effects are being seen by the seismic velocities. With knowledge of the density anomalies which are thermal and compositional (or mineralogical), one can produce a model of mantle flow. This seems a promising approach to take, if we wish to assess whether we can use measurements of anisotropy to determine flow in the mantle. For instance, if the flow is fairly constant over time and shear strains are fairly large ($\gtrsim 1$, perhaps) then current mineral physics understanding suggests we could observe LPO, providing the strain rate is high enough and dislocation creep is occurring. If, on the other hand, strain rates predicted by such inversions are much lower, then perhaps SPO is the likely mechanism.

A further step to take with such an approach is to directly incorporate experimentally or theoretically derived slip system activities for a mono- or polymineralic assemblage of grains and perform VPSC calculations as above. The texture will be more complicated, and likely weaker, but in theory more 'realistic'. This does depend hugely on the flow model being used, though tests on producing a synthetic seismic model from a global flow model by Bull et al. (2010) suggest that the input and recovered strain fields are usually $<20°$ apart. This is encouraging from the perspective of hoping to be able to one day map deformation from anisotropy, but adequate seismic coverage will long be a problem, as discussed in section 6.1.

6. Linking observations to physical processes

If the measurement of seismic anisotropy is to be useful in studying the dynamics of the lowermost mantle, then we need a close understanding of the rheology of mantle materials at CMB conditions. Section 3 discussed that we are still some way from fully understanding how to 'measure' dynamics in D$''$ using seismic anisotropy, but we are now at the stage where our inferences are informed by a great deal of work on the properties of lowermost mantle minerals. In the first instance, seismic anisotropy can be used to evaluate a number of different mechanisms which might cause it.

6.1. Inferring SPO and TTI

A simple mechanism to produce lower mantle anisotropy which cannot at present be ruled out is SPO. This has been the preferred interpretation in a number of studies (*e.g.*, Kendall and Silver, 1998; Lay et al., 1998; Karato, 1998), which model the expected bulk anisotropy for isotropic inclusions of material with a contrasting V_S in an isotropic medium. Kendall and Silver (1998), for instance, use the effective medium theory of Tandon and Weng (1984) to predict the shear wave splitting caused by horizontal rays travelling through a medium with oriented spheroidal inclusions. Whilst high-velocity inclusions are unlikely to be a mechanism which can match the observations (as the inclusions would need to have $V_{\mathrm{S_{inc}}} \gtrsim 13$ km s^{-1}), melt-filled inclusions ($V_{\mathrm{S_{inc}}} = 0$) can produce $\delta V_\mathrm{S} = 2\,\%$ with a melt fraction of just $0.01\,\%$ for oblate spheroidal inclusions. Moore et al. (2004) show a D$''$ with horizontal sub-wavelength layering of heterogeneous material can produce synthetics compatible with observations in certain regions. Both studies suggest that SPO—especially of melt—is an efficient way of producing anisotropy without much reducing the bulk average V_S (Kendall and Silver, 1996).

If we assume that SPO is the cause for an observed anisotropy, then this usually implies that the style of anisotropy is TTI (see section 4). Because of the high symmetry of TTI, two near-perpendicular azimuths of shear waves are sufficient to characterise the orientation of the symmetry axis (or plane of isotropy), as five independent elastic constants describe such a system and the local $\langle V_\mathrm{S} \rangle$ can be assumed.

One simplistic way to infer the orientation of the TTI fabric is to assume a case where Thomsen's (1986) parameters $\delta \approx \epsilon$, hence the fast orientation of a wave split by such a medium is always in the plane of isotropy for waves not perpendicular to the plane. Therefore a simple geometrical calculation to find the common plane of the fast orientations in the ray frame ϕ' can be used. Nowacki et al. (2010) use this to calculate the TTI planes of isotropy beneath the Caribbean and western USA (Figure 17). Figure 18 illustrates the nominally simple geometry for region 'E' in this study.

An alternative method used by Wookey and Kendall (2008) to estimate the orientation of the TTI plane of isotropy for two orthogonal ray paths beneath Siberia can be summarised as: (1) take a set of elastic constants C_{ij} for a TI system, with vertical V_S and V_P defined by a global 1–D velocity model (Kennett et al., 1995); (2) rotate these constants about all three cartesian axes and compute δV_S (and hence δt) and ϕ' at each point; (3) output the orientations which produce $(\phi', \delta t)$ which are compatible with the observations. This inversion has the advantage that it can be simply extended for any set of elastic constants, and lies between analytic solutions from shear wave splitting measurements and inversions for the full elastic tensor, which would likely be poorly constrained.

6.2. Implications of SPO and TTI

If our assumption that the lowermost mantle shows a variable TTI type of anisotropy is correct—and it is worth noting that no studies as yet are incompatible with this symmetry—then what does this imply for the dynamics within and above D″? As discussed in the previous section, various authors have shown that SPO of melt pockets (or other low V_S inclusions) at the CMB could cause this, and this then begs the question as to where these melts come from. A possibility mooted by Knittle and Jeanloz (1987) was that reaction between core and mantle materials would lead to inclusions of Fe-rich products (*e.g.*, FeO, FeSi) in D″ (Kendall and Silver, 1998). However, the bulk reduction in V_{SH} from this does not match observations, hence is an unlikely scenario. As mentioned in section 4, Stixrude et al. (2009), for example, suggest that silicate melts might be present in the lowermost mantle at temperatures as low as 4000 K. Just 0.01 % melt could be compatible with observations given the bulk sound velocity is predicted to be around 10.9 $\mathrm{km\,s^{-1}}$.

If such models are accurate, then we require knowledge of how the inclusions—partially or wholly molten, or simply of contrasting velocity—align in response to flow, to make geodynamical inferences. To first order, weaker inclusions in a stronger matrix align parallel to the strain ellipse's long axis (*i.e.*, the shear plane) when the strain is high ($\gamma > 1$). Hence for the cases where we have two azimuths (in the Caribbean and Siberia), we would predict flow dipping between 26–55° roughly to the south in D″. These steep angles seem somewhat unlikely for high strains, given that flow right at the CMB must be horizontal, but cannot necessarily be precluded.

Contrary to this first-order approximation, weak inclusions apparently rotate when sheared so that they are no longer parallel to the finite strain ellipse, as noted by Karato (1998). Numerous experiments—chiefly on olivine-MORB samples—indicate that shear bands of melt align antithetic to the shear plane at an angle of ∼20–40° (Kohlstedt and Zimmerman, 1996; Holtzman et al., 2003a,b). Taking the example of the regions studied by Wookey and Kendall (2008) and Nowacki et al. (2010), this melt orientation predicts horizontal shear to the north or northwest in western USA, and gently dipping flow to the south elsewhere in the Caribbean and Siberia. Figure 19 shows this situation with the shear wave anisotropy predicted by sensible lowermost mantle parameters, where melt inclusions dip 25° southward, but due to northward flow. In the Caribbean, geodynamical calculations of the flow beneath subducting slabs would generally agree rather with east–west flow for a north–south-striking plate (McNamara et al., 2003), but at least this model seems physically possible.

The known mineral phases present at the CMB do not show hexagonal symmetry, however an alternative explanation for TTI would be the alignment of one crystallographic axis of some anisotropic mineral phase, with the other axes random. As an artificial example, Figure 20 shows the case where an aggregate of ppv shows alignment of c-axes, but the a- and b-axes are otherwise randomly oriented. This might correspond to slip on the (001) plane along both the [100] and [010] directions. This leads to TI with the symmetry axis parallel to the c-axis, where the fast shear wave is within the TI plane.

6.3. Inferring orthorhombic and higher symmetries

Whilst at present TTI cannot be ruled out as causative of the observed seismic anisotropy in D″, a more general orthorhombic symmetry—such as that caused by alignment of orthorhombic crystals—is a more likely mechanism. Equally, cubic and lower symmetries can also produce the observed patterns of anisotropy. However, it is unlikely that distinguishing such a highly symmetric type of anisotropy will be possible with the current earthquake and seismometer geometries for some time, so assuming that orthorhombic anisotropy is the lowest symmetry likely to exist is, for now, a necessary step.

So far, no studies have been able to uniquely infer the orientation of an orthorhombic symmetry, because only measurements of D″ anisotropy along two directions have been made. However, Wookey and Kendall (2008) and Nowacki et al. (2010) use two azimuths and the technique described in Section 6.1 to test the orientations of different candidate orthorhombic systems beneath the Caribbean and Siberia. In the case of using two azimuths of measurements, one normally finds that two sets of planes are compatible. Figure 21 shows an example of fitting possible orientations of different (orthorhombic) elastic constants to measurements made beneath the three regions of Nowacki et al. (2010). They use a set of constants obtained by Yamazaki et al. (2006), who deform $CaIrO_3$ (same structure as $MgSiO_3$-post-perovskite), and find that the [100](010) slip system is dominant. The elastic constants are referenced to the shear plane and slip direction imposed upon the deformation, so we can directly infer in which direction a material which behaves in this way is being sheared.

6.4. Inferring deformation in D″

We measure D″ anisotropy in the hope that it can provide information about the manner in which it is deforming, and hence how the mantle moves at depths. In order to estimate flow or strain from anisotropy, we must integrate our understanding of the cause of anisotropy, the orientation of the assumed anisotropy type, our knowledge of the rheology of the medium, and the response of the shear direction to the potentially changing flow field. Figure 22 illustrates the many steps involved in getting from observations to predictions of deformation, and the many assumptions which are made along the way.

At present, the response of D″ materials to deformation is not well known, hence early attempts at inferring flow from measurements of seismic anisotropy were necessarily general. Beneath the circum-Pacific subduction zones where flow is assumed to be horizontal at the CMB, the global ξ models of Panning and Romanowicz (2004, 2006) show $V_{\mathrm{SH}} > V_{\mathrm{SV}}$, and thus it has been interpreted that likely mechanisms in response to shear in D″ mineral should produce fast orientations parallel to the shear plane. This then may lead to the inference that beneath the central Pacific, the change of $\xi > 1$ to $\xi < 1$ corresponds to vertical flow (*e.g.*, Kawai and Geller, 2010) or some sort of shearing in different horizontal directions (*e.g.*, Pulliam and Sen, 1998). Clearly, whilst there is short scale variability in the signal anyway, determining the first-order flow field from an educated guess is an understandable first step which we should attempt to improve upon.

In fact, this point highlights one of the current shortcomings in our addressing of the problem of using seismic anisotropy to map deformation. At present, we are limited to using 'best guess' estimates of the flow field in certain areas at the CMB (specifically, where the ancient Farallon slab is presumed to be sinking to the CMB beneath North and Central America, and to some extent other circum-Pacific subduction zones) to argue for and against different mechanisms for producing seismic anisotropy. For instance, Yamazaki and Karato (2007) prefer an explanation for D″ anisotropy of the LPO of a mixture of (Mg,Fe)O and $MgSiO_3$-post-perovskite because horizontal shear would give a horizontally-polarised fast shear wave for this case, which is the sort of deformation postulated beneath deep slabs. They then argue that SPO of melt inclusions oriented vertically is the likeliest case for the central Pacific, because flow there is probably vertical and in higher-temperature material. If the CMB is considered an impenetrable free slip surface, then why should flow not also be mainly vertical in the very lowermost mantle beneath a downwelling as well as an upwelling? Whilst these first-order explanations are sensible, they are only an initial idea about flow, hence using this to constrain LPO and infer the presence of melt makes a large stride in assumptions which we must eventually address with direct observations of lowermost mantle rheology.

Nonetheless, many authors have inferred different flow regimes at the CMB based on seismic anisotropy. Early work (*e.g.*, Vinnik et al. 1995; Lay and Young 1991; Ritsema et al. 1998) attributed anisotropy to stratification or LPO on the basis of the expected flow field near the CMB. Later, Kendall and Silver (1996), for instance, identify slab material which is laid down in piles parallel to the CMB as a cause of SPO. Recently, dual-azimuth splitting measurements were used in combination with global V_S tomography to infer that north-south flow beneath Siberia is the likely cause of anisotropy due to LPO of ppv (Wookey and Kendall, 2008). Similarly, Nowacki et al. (2010) infer that an LPO of ppv whereby the (001) planes align parallel to shear is most likely beneath the Farallon slab because of first-order flow arguments, and then extend the argument to suggest that shear planes dip towards the downwelling centre, analogous to the situation in mid-ocean spreading centres (Blackman et al., 1996), and supported by general-case geodynamic calculations (McNamara et al., 2002)

Future advances in incorporating all our current understanding of the behaviour of the constituents of the lowermost mantle into linking observations and dynamics will become incrementally better. These early attempts at measuring the flow of the deepest mantle should be surpassed as we use new information which becomes available from increasingly advanced experimental and numerical techniques for studying seismic anisotropy, flow, geodynamics and mineral physics.

7. Conclusions and future directions

In this review, we have presented the current state of studies which aim to use seismic anisotropy to discover the flow in the deepest mantle, and the many other fields which feed into this. It seems that we are moving from an early phase of D″ study into a more mature field, where the number of observations is now becoming limited by the location of seismic stations. As we look to the future, projects to increase global coverage of seismometers will benefit all studies of the Earth's interior, but especially that of the lowermost mantle. With this increased coverage, the prospect of using more advanced techniques to take advantage is an exciting one which may yet yield even harder questions that we currently try to answer.

One such technique that must be further explored with new datasets is the full inversion for the elastic tensor using the full seismic waveform. Recent advances towards this necessarily assume a simple anisotropy, but this can be relaxed as data coverage improves. However, as for global inversions for simple anisotropy, upper mantle and crustal corrections will be a problem. At the same time, existing global datasets—as used for global tomography, for example—might be exploited to move from regional shear wave splitting studies to global ones. This will require either a new, robust way of analysing shear wave splitting, which is still the most unequivocal of observations of anisotropy, or the further automation and quality control of standard techniques. Shear wave splitting 'tomography' is another technique which will likely prove important in the future.

Whilst seismological observations will be our primary test of models of D″ flow and anisotropy for some time, advances must be made in mineral physics and geodynamics if we are to improve. Studies of deformation in likely lowermost mantle mineral assemblages will hopefully go some way in the future to reducing the ambiguity regarding how to translate anisotropy to flow, and global mantle flow models may be able to become predictors of anisotropy with such knowledge.

Acknowledgements

The authors are thankful to Andrew Walker for insightful comments on the manuscript. AJN was supported by NERC.

References

Adams, D., Oganov, A., 2006. Ab initio molecular dynamics study of $CaSiO_3$ perovskite at P-T conditions of Earth's lower mantle. Phys. Rev. B 73, 184106.

Ammann, M.W., Brodholt, J.P., Wookey, J., Dobson, D.P., 2010. First-principles constraints on diffusion in lower-mantle minerals and a weak D″ layer. Nature 465, 462–465.

Andrault, D., Muñoz, M., Bolfan-Casanova, N., Guignot, N., Perrillat, J.P., Aquilanti, G., Pascarelli, S., 2010. Experimental evidence for perovskite and post-perovskite coexistence throughout the whole D″ region. Earth Planet Sci Lett 293, 90–96.

Becker, T.W., Boschi, L., 2002. A comparison of tomographic and geodynamic mantle models. Geochem Geophy Geosy 3, 1003.

Blackman, D., Kendall, J.M., Dawson, P., Wenk, H.R., Boyce, D., Morgan, J., 1996. Teleseismic imaging of subaxial flow at mid-ocean ridges: Traveltime effects of anisotropic mineral texture in the mantle. Geophys J Int 127, 415–426.

Bull, A.L., McNamara, A.K., Becker, T.W., Ritsema, J., 2010. Global scale models of the mantle flow field predicted by synthetic tomography models. Phys. Earth Planet. Inter. 182, 129–138.

Bullen, K., 1940. The problem of the Earth's density variation. B Seismol Soc Am .

Bullen, K., 1949. An Earth model based on a compressibility-pressure hypothesis.

Carrez, P., Ferre, D., Cordier, P., 2007. Implications for plastic flow in the deep mantle from modelling dislocations in $MgSiO_3$ minerals. Nature 446, 68–70.

Carrez, P., Ferre, D., Cordier, P., 2009. Peierls-Nabarro modelling of dislocations in MgO from ambient pressure to 100 GPa. Model Simul Mater Sc 17, 035010.

Catalli, K., Shim, S.H., Prakapenka, V.B., 2009. Thickness and Clapeyron slope of the post-perovskite boundary. Nature 462, 782–U101.

Chevrot, S., 2000. Multichannel analysis of shear wave splitting. J Geophys Res-Sol Ea 105, 21579–21590.

Cordier, P., Ungar, T., Zsoldos, L., Tichy, G., 2004. Dislocation creep in $MgSiO_3$ perovskite at conditions of the Earth's uppermost lower mantle. Nature 428, 837–840.

Ding, X., Helmberger, D., 1997. Modelling D″ structure beneath Central America with broadband seismic data. Phys. Earth Planet. Inter. 101, 245–270.

Durham, W., Weidner, D., Karato, S. Wang, Y. 2002. New developments in deformation experiments at high pressure, in: Karato, S., Wenk, H. (Eds.), Plastic Deformation of Minerals and Rocks. volume 51 of *Reviews in Mineralogy & Geochemistry*, pp. 21–49. Mineralogical Society of America, San Francisco, USA.

Dziewonski, A., Anderson, D., 1981. Preliminary reference Earth model. Phys. Earth Planet. Inter. 25, 297–356.

Ford, S., Garnero, E.J., McNamara, A.K., 2006. A strong lateral shear velocity gradient and anisotropy heterogeneity in the lowermost mantle beneath the southern Pacific. J Geophys Res-Sol Ea 111, B03306.

Fouch, M.J., Fischer, K.M., Wysession, M., 2001. Lowermost mantle anisotropy beneath the Pacific: Imaging the source of the Hawaiian plume. Earth Planet Sci Lett 190, 167–180.

Fukao, Y., 1984. Evidence from core-reflected shear-waves for anisotropy in the Earth's mantle. Nature 309, 695–698.

Garnero, E.J., Lay, T., 1997. Lateral variations in lowermost mantle shear wave anisotropy beneath the north Pacific and Alaska. J Geophys Res-Sol Ea 102, 8121–8135.

Garnero, E.J., Lay, T., 2003. D″ shear velocity heterogeneity, anisotropy and discontinuity structure beneath the Caribbean and Central America. Phys Earth Planet Inter 140, 219–242.

Garnero, E.J., Maupin, V., Lay, T., Fouch, M.J., 2004a. Variable azimuthal anisotropy in Earth's lowermost mantle. Science 306, 259–261.

Garnero, E.J., Moore, M., Lay, T., Fouch, M.J., 2004b. Isotropy or weak vertical transverse isotropy in D″ beneath the Atlantic Ocean. J Geophys Res-Sol Ea 109, B08308.

Garnero, E.J., Revenaugh, J., Williams, Q., Lay, T., Kellogg, L., 1998. Ultralow velocity zone at the core–mantle boundary, in: Gurnis, M., Wysession, M.E., Knittle, E., Buffett, B.A. (Eds.), The Core–Mantle Boundary Region. American Geophysical Union. Geodynamics Series, pp. 319–334.

Guignot, N., Andrault, D., Morard, G., Bolfan-Casanova, N., Mezouar, M., 2007. Thermoelastic properties of post-perovskite phase $MgSiO_3$ determined experimentally at core-mantle boundary P-T conditions. Earth Planet Sci Lett 256, 162–168.

Hall, S., Kendall, J.M., 2001. Constraining the interpretation of AVOA for fracture characterisation, in: Ikelle, L., Gangi, A. (Eds.), Anisotropy 2000: Fractures, Converted Waves, and Case Studies. Proceedings of 9$^{\text{th}}$ International Workshop on Seismic Anisotropy (9IWSA). Society of Exploration Geophysicists, Tulsa, USA. volume 6 of *Open File Publications*, pp. 107–144.

Hall, S., Kendall, J.M., van der Baan, M., 2004. Some comments on the effects of lower-mantle anisotropy on SKS and SKKS phases. Phys. Earth Planet. Inter. 146, 469–481.

Hedlin, M., Shearer, P., Earle, P., 1997. Seismic evidence for small-scale heterogeneity throughout the Earth's mantle. Nature 387, 145–150.

Hernlund, J.W., 2010. On the interaction of the geotherm with a post-perovskite phase transition in the deep mantle. Phys. Earth Planet. Inter. 180, 222–234.

Hernlund, J.W., Thomas, C. Tackley, P.J., 2005. A doubling of the post-perovskite phase boundary and structure of the Earth's lowermost mantle. Nature 434, 882–886.

Hirose, K., 2006. Postperovskite phase transition and its geophysical implications. Rev. Geophys. 44, RG3001.

Hirose, K., 2007. Discovery of post-perovskite phase transition and the nature of D″ layer, in: Hirose, K., Brodholt, J., Lay, T., Yuen, D.A. (Eds.), Post-Perovksite: The Last Mantle Phase Transition. American Geophysical Union. Geophysical Monograph, pp. 19–35.

Hirose, K., Fei, Y., Ma, Y., Mao, H., 1999. The fate of subducted basaltic crust in the Earth's lower mantle. Nature 397, 53–56.

Hirose, K., Nagaya, Y., Merkel, S., Ohishi, Y., 2010. Deformation of $MnGeO_3$ post-perovskite at lower mantle pressure and temperature. Geophys Res Lett 37, 1–5.

Hirose, K., Sinmyo, R., Sata, N., Ohishi, Y., 2006. Determination of post-perovskite phase transition boundary in $MgSiO_3$ using Au and MgO pressure standards. Geophys Res Lett 33, L01310.

Hirose, K., Takafuji, N., Sata, N., Ohishi, Y., 2005. Phase transition and density of subducted MORB crust in the lower mantle. Earth Planet Sci Lett 237, 239–251.

Holtzman, B., Groebner, N., Zimmerman, M., Ginsberg, S., Kohlstedt, D., 2003a. Stress-driven melt segregation in partially molten rocks. Geochem Geophy Geosy 4, 8607.

Holtzman, B., Kohlstedt, D., Zimmerman, M., Heidelbach, F., Hiraga, T., Hustoft, J.W., 2003b. Melt segregation and strain partitioning: Implications for seismic anisotropy and mantle flow. Science 301, 1227–1230.

Holtzman, B.K., Kendall, J.M., 2010. Organized melt, seismic anisotropy, and plate boundary lubrication. Geochem Geophy Geosy 11, Q0AB06.

Hudson, J., 1980a. The excitation and propagation of elastic waves. Cambridge University Press, Cambridge, U.K.

Hudson, J., 1980b. Overall properties of a cracked solid. Math. Proc. Camb. Phil. Soc. 88, 371–384.

Iitaka, T., Hirose, K., Kawamura, K., Murakami, M., 2004. The elasticity of the $MgSiO_3$ post-perovskite phase in the Earth's lowermost mantle. Nature 430, 442–445.

Karato, S., 1998. Some remarks on the origin of seismic anisotropy in the D″ layer. Earth Planets Space 50, 1019–1028.

Karki, B., Stixrude, L., Crain, J., 1997a. Ab initio elasticity of three high-pressure polymorphs of silica. Geophys Res Lett 24, 3269–3272.

Karki, B., Warren, M., Stixrude, L., Ackland, G., Crain, J., 1997b. Ab initio studies of high-pressure structural transformations in silica. Phys. Rev. B 55, 3465–3471.

Karki, B., Wentzcovitch, R., de Gironcoli, S., Baroni, S., 1999. First-principles determination of elastic anisotropy and wave velocities of MgO at lower mantle conditions. Science 286, 1705–1707.

Kawai, K., Geller, R.J., 2010. The vertical flow in the lowermost mantle beneath the Pacific from inversion of seismic waveforms for anisotropic structure. Earth Planet Sci Lett 297, 190–198.

Kendall, J.M., 2000. Seismic anisotropy in the boundary layers of the mantle, in: Karato, S., Forte, A., Liebermann, R.C., Masters, G., Stixrude, L. (Eds.), Earth's Deep Interior: Mineral Physics and Tomography from the Atomic to the Global Scale. American Geophysical Union, Washington, D.C., USA. volume 117 of *Geophysical Monograph*, pp. 133–159.

Kendall, J.M., Nangini, C., 1996. Lateral variations in D″ below the Caribbean. Geophys Res Lett 23, 399–402.

Kendall, J.M., Silver, P.G., 1996. Constraints from seismic anisotropy on the nature of the lowermost mantle. Nature 381, 409–412.

Kendall, J.M., Silver, P.G., 1998. Investigating causes of D″ anisotropy, in: Gurnis, M., Wysession, M.E., Knittle, E., Buffett, B.A. (Eds.), The Core–Mantle Boundary Region. American Geophysical Union. Geodynamics Series, pp. 97–118.

Kennett, B., Engdahl, E., Buland, R., 1995. Constraints on seismic velocities in the Earth from travel-times. Geophys J Int 122, 108–124.

Kesson, S., Gerald, J.F., Shelley, J., 1998. Mineralogy and dynamics of a pyrolite lower mantle. Nature 393, 252–255.

Knittle, E., Jeanloz, R., 1987. Synthesis and equation of state of (Mg,Fe)SiO_3 perovskite to over 100 gigapascals. Science 235, 668–670.

Koci, L., Vitos, L., Ahuja, R., 2007. Ab initio calculations of the elastic properties of ferropericlase

$Mg_{1-x}Fe_xO$ ($x \leq 0.25$). Phys. Earth Planet. Inter. 164, 177–185.

Kohlstedt, D., Zimmerman, M., 1996. Rheology of partially molten mantle rocks. Annu Rev Earth Pl Sc 24, 41–62.

Kohn, W., Sham, L., 1965. Self-consistent equations including exchange and correlation effects. Phys. Rev 140, A1133–A1138.

Komabayashi, T., Hirose, K., Nagaya, Y., Sugimura, E., Ohishi, Y., 2010. High-temperature compression of ferropericlase and the effect of temperature on iron spin transition. Earth Planet Sci Lett 297, 691–699.

Komatitsch, D., Vinnik, L.P., Chevrot, S., 2010. SHdiff-SVdiff splitting in an isotropic Earth. J Geophys Res-Sol Ea 115, B07312.

Kubo, A., Kiefei, B., Shim, S.H., Shen, G., Prakapenka, V.B., Duffy, T.S., 2008. Rietveld structure refinement of $MgGeO_3$ post-perovskite phase to 1 Mbar. Am Mineral 93, 965–976.

Kustowski, B., Ekstrom, G., Dziewonski, A., 2008. Anisotropic shear-wave velocity structure of the Earth's mantle: A global model. J Geophys Res-Sol Ea 113, B06306.

Lay, T., Helmberger, D., 1983. The shear-wave velocity-gradient at the base of the mantle. J Geophys Res 88, 8160–8170.

Lay, T., Williams, Q., Garnero, E.J., Kellogg, L., Wysession, M.E., 1998. Seismic wave anisotropy in the D″ region and its implications, in: Gurnis, M., Wysession, M.E., Knittle, E., Buffett, B.A. (Eds.), The Core–Mantle Boundary Region. American Geophysical Union, Washington, D.C., USA. Geodynamics Series 28, pp. 299–318.

Lay, T., Young, C., 1991. Analysis of seismic SV waves in the core's penumbra. Geophys Res Lett 18, 1373–1376.

Lebensohn, R., Tomé, C., 1993. A self-consistent anisotropic approach for the simulation of plastic-deformation and texture development of polycrystals—application to zirconium alloys. Acta Metallurgica Et Materialia 41, 2611–2624.

Lekic, V., Panning, M., Romanowicz, B., 2010. A simple method for improving crustal corrections in waveform tomography. Geophys J Int 182, 265–278.

Li, L., Weidner, D.J., Brodholt, J.P., Alfe, D., Price, G.D., Caracas, R., Wentzcovitch, R., 2006a. Elasticity of $CaSiO_3$ perovskite at high pressure and high temperature. Phys. Earth Planet. Inter. 155, 249–259.

Li, L., Weidner, D.J., Brodholt, J.P., Alfe, D., Price, G.D., Caracas, R., Wentzcovitch, R., 2006b. Phase stability of $CaSiO_3$ perovskite at high pressure and temperature: Insights from ab initio molecular dynamics. Phys. Earth Planet. Inter. 155, 260–268.

Lin, J.F., Tsuchiya, T., 2008. Spin transition of iron in the Earth's lower mantle. Phys. Earth Planet. Inter. 170, 248–259.

Lithgow-Bertelloni, C., Richards, M., 1998. The dynamics of Cenozoic and Mesozoic plate motions. Rev. Geophys. 36, 27–78.

Long, M.D., 2009. Complex anisotropy in D″ beneath the eastern pacific from SKS-SKKS splitting discrepancies. Earth Planet Sci Lett 283, 181–189.

Long, M.D., Xiao, X., Jiang, Z., Evans, B., Karato, S., 2006. Lattice preferred orientation in deformed polycrystalline (Mg,Fe)O and implications for seismic anisotropy in D″. Phys. Earth Planet. Inter. 156, 75–88.

Mainprice, D., Silver, P., 1993. Interpretation of SKS-waves using samples from the subcontinental lithosphere.

Mainprice, D., Tommasi, A., Ferre, D., Carrez, P., Cordier, P., 2008. Predicted glide systems and crystal preferred orientations of polycrystalline silicate Mg-perovskite at high pressure: Implications for the seismic anisotropy in the lower mantle. Earth Planet Sci Lett 271, 135–144.

Mao, W.L., Meng, Y., Mao, H., 2010. Elastic anisotropy of ferromagnesian post-perovskite in Earth's D″ layer. Phys. Earth Planet. Inter. 180, 203–208.

Marquardt, H., Speziale, S., Reichmann, H.J., Frost, D.J., Schilling, F.R., 2009. Single-crystal elasticity of $(Mg_{0.9}Fe_{0.1})O$ to 81 GPa. Earth Planet Sci Lett 287, 345–352.

Matzel, E., Sen, M., Grand, S.P., 1996. Evidence for anisotropy in the deep mantle beneath Alaska. Geophys Res Lett 23, 2417–2420.

Maupin, V., 1994. On the possibility of anisotropy in the D'' layer as inferred from the polarization of diffracted S waves. Phys. Earth Planet. Inter. 87, 1–32.

Maupin, V., Garnero, E.J., Lay, T., Fouch, M.J., 2005. Azimuthal anisotropy in the D'' layer beneath the Caribbean. J Geophys Res-Sol Ea 110, B08301.

McDonough, W., Sun, S., 1995. The composition of the Earth. Chem Geol 120, 223–253.

McNamara, A., van Keken, P., Karato, S., 2002. Development of anisotropic structure in the Earth's lower mantle by solid-state convection. Nature 416, 310–314.

McNamara, A.K., van Keken, P., Karato, S., 2003. Development of finite strain in the convecting lower mantle and its implications for seismic anisotropy. J Geophys Res-Sol Ea 108, 2230.

Meade, C., Silver, P.G., Kaneshima, S., 1995. Laboratory and seismological observations of lower mantle isotropy. Geophys Res Lett 22, 1293–1296.

Merkel, S., Kubo, A., Miyagi, L., Speziale, S., Duffy, T.S., Mao, H., Wenk, H.R., 2006. Plastic deformation of $MgGeO_3$ post-perovskite at lower mantle pressures. Science 311, 644–646.

Merkel, S., McNamara, A.K., Kubo, A., Speziale, S., Miyagi, L., Meng, Y., Duffy, T.S., Wenk, H.R., 2007. Deformation of $(Mg,Fe)SiO_3$ post-perovskite and D'' anisotropy. Science 316, 1729–1732.

Merkel, S., Wenk, H.R., Badro, J., Montagnac, G., Gillet, P., Mao, H., Hemley, R., 2003. Deformation of $(Mg_{0.9},Fe_{0.1})SiO_3$ Perovskite aggregates up to 32 GPa. Earth Planet Sci Lett 209, 351–360.

Merkel, S., Wenk, H.R., Shu, J., Shen, G., Gillet, P., Mao, H., Hemley, R., 2002. Deformation of polycrystalline MgO at pressures of the lower mantle. J Geophys Res-Sol Ea 107, 2271.

Metsue, A., Carrez, P., Mainprice, D., Cordier, P., 2009. Numerical modelling of dislocations and deformation mechanisms in $CaIrO_3$ and $MgGeO_3$ post-perovskites—Comparison with $MgSiO_3$ post-perovskite.

Mitrovica, J.X., Forte, A.M., 2004. A new inference of mantle viscosity based upon joint inversion of convection and glacial isostatic adjustment data. Earth Planet Sci Lett 225, 177–189.

Miyagi, L., Kanitpanyacharoen, W., Kaercher, P., Lee, K.K.M., Wenk, H.R., 2010. Slip systems in $MgSiO_3$ post-perovskite: Implications for D'' anisotropy. Science 329, 1639–1641.

Miyagi, L., Nishlyama, N., Wang, Y., Kubo, A., West, D.V., Cava, R.J., Duffy, T.S., Wenk, H.R., 2008. Deformation and texture development in $CaIrO_3$ post-perovskite phase up to 6 GPa and 1300 K. Earth Planet Sci Lett 268, 515–525.

Montagner, J.P., Kennett, B., 1996. How to reconcile body-wave and normal-mode reference earth models. Geophys J Int 125, 229–248.

Montelli, R., Nolet, G., Dahlen, F., Masters, G., Engdahl, E., Hung, S., 2004. Finite-frequency tomography reveals a variety of plumes in the mantle. Science 303, 338–343.

Moore, M., Garnero, E.J., Lay, T., Williams, Q., 2004. Shear wave splitting and waveform complexity for lowermost mantle structures with low-velocity lamellae and transverse isotropy. J Geophys Res-Sol Ea 109, B02319.

Murakami, M., Hirose, K., Kawamura, K., Sata, N., Ohishi, Y., 2004. Post-perovskite phase transition in $MgSiO_3$. Science 304, 855–858.

Murakami, M., Hirose, K., Sata, N., Ohishi, Y., 2005. Post-perovskite phase transition and mineral chemistry in the pyrolitic lowermost mantle. Geophys Res Lett 32, L03304.

Niu, F., Perez, A., 2004. Seismic anisotropy in the lower mantle: A comparison of waveform splitting of SKS and SKKS. Geophys Res Lett 31, L24612.

Niwa, K., Yagi, T., Ohgushi, K., Merkel, S., Miyajima, N., Kikegawa, T., 2007. Lattice preferred orientation in $CaIrO_3$ perovskite and post-perovskite formed by plastic deformation under pressure. Phys Chem Miner 34, 679–686.

Nowacki, A., Wookey, J., Kendall, J.M., 2010. Deformation of the lowermost mantle from seismic anisotropy. Nature 467, 1091–1094.

Nye, J., 1985. Physical properties of crystals: their representation by tensors and matrices. Oxford science publications, Clarendon Press.

Oganov, A., Brodholt, J., Price, G., 2001. The elastic constants of $MgSiO_3$ perovskite at pressures and temperatures of the Earth's mantle. Nature 411, 934–937.

Oganov, A., Martonak, R., Laio, A., Raiteri, P., Parrinello, M., 2005. Anisotropy of Earth's D'' layer and stacking faults in the $MgSiO_3$ post-perovskite phase. Nature 438, 1142–1144.

Oganov, A., Ono, S., 2004. Theoretical and experimental evidence for a post-perovskite phase of $MgSiO_3$ in Earth's D$''$ layer. Nature 430, 445–448.

Ohta, K., Hirose, K., Lay, T., Sata, N., Ohishi, Y., 2008. Phase transitions in pyrolite and MORB at lowermost mantle conditions: Implications for a MORB-rich pile above the core-mantle boundary. Earth Planet Sci Lett 267, 107–117.

Ohtani, E., Sakai, T., 2008. Recent advances in the study of mantle phase transitions. Phys. Earth Planet. Inter. 170, 240–247.

Okada, T., Yagi, T., Niwa, K., Kikegawa, T., 2010. Lattice-preferred orientations in post-perovskite-type $MgGeO_3$ formed by transformations from different pre-phases. Phys. Earth Planet. Inter. 180, 195–202.

Ono, S., Ito, E., Katsura, T., 2001. Mineralogy of subducted basaltic crust (MORB) from 25 to 37 GPa, and chemical heterogeneity of the lower mantle. Earth Planet Sci Lett 190, 57–63.

Ono, S., Oganov, A., 2005. In situ observations of phase transition between perovskite and $CaIrO_3$-type phase in $MgSiO_3$ and pyrolitic mantle composition. Earth Planet Sci Lett 236, 914–932.

Panning, M., Romanowicz, B., 2004. Inferences on flow at the base of Earth's mantle based on seismic anisotropy. Science 303, 351–353.

Panning, M., Romanowicz, B., 2006. A three-dimensional radially anisotropic model of shear velocity in the whole mantle. Geophys J Int 167, 361–379.

Perdew, J.P., Ruzsinszky, A., 2010. Density functional theory of electronic structure: A short course for mineralogists and geophysicists, in: Wentzcovitch, R., Stixrude, L. (Eds.), Theoretical And Computational Methods In Mineral Physics: Geophysical Applications. volume 71 of *Reviews in Mineralogy & Geochemistry*, pp. 1–18.

Pulliam, J., Sen, M., 1998. Seismic anisotropy in the core-mantle transition zone. Geophys J Int 135, 113–128.

Restivo, A., Helffrich, G., 2006. Core-mantle boundary structure investigated using SKS and SKKS polarization anomalies. Geophys J Int 165, 288–302.

Ricolleau, A., Fei, Y., Cottrell, E., Watson, H., Deng, L., Zhang, L., Fiquet, G., Auzende, A.L., Roskosz, M., Morard, G., Prakapenka, V.B., 2009. Density profile of pyrolite under the lower mantle conditions. Geophys Res Lett 36, L06302.

Ringwood, A., 1962. A model for the upper mantle. J Geophys Res 67, 857–867.

Ritsema, J., 2000. Evidence for shear velocity anisotropy in the lowermost mantle beneath the Indian Ocean. Geophys Res Lett 27, 1041–1044.

Ritsema, J., van Heijst, H., Woodhouse, J.H., 1999. Complex shear wave velocity structure imaged beneath Africa and Iceland. Science 286, 1925–1928.

Ritsema, J., Lay, T., Garnero, E.J., Benz, H., 1998. Seismic anisotropy in the lowermost mantle beneath the Pacific. Geophys Res Lett 25, 1229–1232.

Rokosky, J.M., Lay, T., Garnero, E.J., 2006. Small-scale lateral variations in azimuthally anisotropic D$''$ structure beneath the Cocos Plate. Earth Planet Sci Lett 248, 411–425.

Rokosky, J.M., Lay, T., Garnero, E.J., Russell, S., 2004. High-resolution investigation of shear wave anisotropy in D$''$ beneath the Cocos Plate. Geophys Res Lett 31, L07605.

Royer, D., Dieulesaint, E., 2000. Elastic Waves in Solids I: Free and guided propagation. Advanced texts in physics, Springer.

Russell, S., Lay, T., Garnero, E.J., 1998. Seismic evidence for small-scale dynamics in the lowermost mantle at the root of the Hawaiian hotspot. Nature 396, 255–258.

Russell, S., Lay, T., Garnero, E.J., 1999. Small-scale lateral shear velocity and anisotropy heterogeneity near the core-mantle boundary beneath the central Pacific imaged using broadband ScS waves. J Geophys Res-Sol Ea 104, 13183–13199.

Rümpker, G., Tommasi, A., Kendall, J.M., 1999. Numerical simulations of depth-dependent anisotropy and frequency-dependent wave propagation effects. J Geophys Res-Sol Ea 104, 23141–23153.

Savage, M., 1999. Seismic anisotropy and mantle deformation: What have we learned from shear wave splitting? Rev. Geophys. 37, 65–106.

Sayers, C., 1992. Elastic anisotropy of short-fibre reinforced composites. Int. J. Solids Structures 100, 4149–4156.

Shim, S.H., 2008. The postperovskite transition. Annu Rev Earth Pl Sc 36, 569–599.

Silver, P.G., Chan, W.W., 1991. Shear-wave splitting and subcontinental mantle deformation. J Geophys Res-Sol Ea 96, 16429–16454.

Silver, P.G., Savage, M., 1994. The interpretation of shear-wave splitting parameters in the presence of two anisotropic layers. Geophys J Int 119, 949–963.

Simmons, N.A., Forte, A.M., Grand, S.P., 2009. Joint seismic, geodynamic and mineral physical constraints on three-dimensional mantle heterogeneity: Implications for the relative importance of thermal versus compositional heterogeneity. Geophys J Int 177, 1284–1304.

Sinmyo, R., Hirose, K., Nishio-Hamane, D., Seto, Y., Fujino, K., Sata, N., Ohishi, Y., 2008. Partitioning of iron between perovskite/postperovskite and ferropericlase in the lower mantle. J Geophys Res-Sol Ea 113, B11204.

Speziale, S., Zha, C., Duffy, T., Hemley, R., Mao, H., 2001. Quasi-hydrostatic compression of magnesium oxide to 52 GPa: Implications for the pressure-volume-temperature equation of state. J Geophys Res-Sol Ea 106, 515–528.

Stackhouse, S., Brodholt, J.P., Price, G.D., 2005a. High temperature elastic anisotropy of the perovskite and post-perovskite Al_2O_3. Geophys Res Lett 32, L13305.

Stackhouse, S., Brodholt, J.P., Price, G.D., 2006. Elastic anisotropy of $FeSiO_3$ end-members of the perovskite and post-perovskite phases. Geophys Res Lett 33, L01304.

Stackhouse, S., Brodholt, J.P., Wookey, J., Kendall, J.M., Price, G.D., 2005b. The effect of temperature on the seismic anisotropy of the perovskite and post-perovskite polymorphs of $MgSiO_3$. Earth Planet Sci Lett 230, 1–10.

Stixrude, L., de Koker, N., Sun, N., Mookherjee, M., Karki, B.B., 2009. Thermodynamics of silicate liquids in the deep Earth. Earth Planet Sci Lett 278, 226–232.

Stixrude, L., Lithgow-Bertelloni, C., Kiefer, B., Fumagalli, P., 2007. Phase stability and shear softening in $CaSiO_3$ perovskite at high pressure. Phys. Rev. B 75, 024108.

Tackley, P., 2000. Mantle convection and plate tectonics: Toward an integrated physical and chemical theory. Science 288, 2002–2007.

Tanaka, S., 2010. Constraints on the core-mantle boundary topography from P4KP-PcP differential travel times. J Geophys Res-Sol Ea 115, B04310.

Tandon, G., Weng, G., 1984. The effect of aspect ratio of inclusions on the elastic properties of unidirectionally aligned composites. Polym Composite 5, 327–333.

Tateno, S., Hirose, K., Sata, N., Ohishi, Y., 2009. Determination of post-perovskite phase transition boundary up to 4400 K and implications for thermal structure in D'' layer. Earth Planet Sci Lett 277, 130–136.

Teanby, N., Kendall, J.M., der Baan, M.V., 2004. Automation of shear-wave splitting measurements using cluster analysis. B Seismol Soc Am 94, 453–463.

Thomas, C., Kendall, J.M., 2002. The lowermost mantle beneath northern Asia - II. Evidence for lower-mantle anisotropy. Geophys J Int 151, 296–308.

Thomas, C., Wookey, J., Simpson, M., 2007. D'' anisotropy beneath Southeast Asia. Geophys Res Lett 34, L04301.

Thomsen, L., 1986. Weak elastic anisotropy. Geophysics 51, 1954–1966.

Tikoff, B., Fossen, H., 1999. Three-dimensional reference deformations and strain facies. Journal of Structural Geology 21, 1497–1512.

Trampert, J., Deschamps, F., Resovsky, J., Yuen, D., 2004. Probabilistic tomography maps chemical heterogeneities throughout the lower mantle. Science 306, 853–856.

Tromp, J., 2001. Inner-core anisotropy and rotation. Annu Rev Earth Pl Sc 29, 47–69.

Trønnes, R.G., 2010. Structure, mineralogy and dynamics of the lowermost mantle. Miner Petrol 99, 243–261.

Tsuchiya, T., 2003. First-principles prediction of the P-V-T equation of state of gold and the 660-km discontinuity in Earth's mantle. J Geophys Res-Sol Ea 108, 2462.

Tsuchiya, T., Tsuchiya, J., Umemoto, K., Wentzcovitch, R., 2004. Phase transition in $MgSiO_3$ perovskite in the earth's lower mantle. Earth Planet Sci Lett 224, 241–248.

Usui, Y., Hiramatsu, Y., Furumoto, M., Kanao, M., 2008. Evidence of seismic anisotropy and a lower temperature condition in the D'' layer beneath Pacific Antarctic Ridge in the Antarctic Ocean. Phys. Earth Planet. Inter. 167, 205–216.

Vinnik, L.P., Breger, L., Romanowicz, B., 1998. Anisotropic structures at the base of the Earth's mantle. Nature 393, 564–567.

Vinnik, L.P., Kind, R., Kosarev, G., Makeyeva, L., 1989. Azimuthal anisotropy in the lithosphere from observations of long-period S-waves. Geophys J Int 99, 549–559.

Vinnik, L.P., Romanowicz, B., Stunff, Y.L., Makeyeva, L., 1995. Seismic anisotropy in the D'' layer. Geophys Res Lett 22, 1657–1660.

Walker, A., Carrez, P., Cordier, P., 2010. Atomic-scale models of dislocation cores in minerals: progress and prospects. Mineral. Mag. 74, 381–413.

Walte, N.P., Heidelbach, F., Miyajima, N., Frost, D.J., 2007. Texture development and TEM analysis of deformed $CaIrO_3$: Implications for the D'' layer at the core-mantle boundary. Geophys Res Lett 34, L08306.

Walte, N.P., Heidelbach, F., Miyajima, N., Frost, D.J., Rubie, D.C., Dobson, D.P., 2009. Transformation textures in post-perovskite: Understanding mantle flow in the D'' layer of the Earth. Geophys Res Lett 36, L04302.

Wang, Y., Wen, L., 2007. Complex seismic anisotropy at the border of a very low velocity province at the base of the Earth's mantle. J Geophys Res-Sol Ea 112, B09305.

Wenk, H.R., Bennett, K., Canova, G., Molinari, A., 1991. Modeling plastic-deformation of peridotite with the self-consistent theory. Journal Of Geophysical Research-Solid Earth And Planets 96, 8337–8349.

Wenk, H.R., Speziale, S., McNamara, A.K., Garnero, E.J., 2006. Modeling lower mantle anisotropy development in a subducting slab. Earth Planet Sci Lett 245, 302–314.

Wentzcovitch, R., Karki, B., Cococcioni, M., de Gironcoli, S., 2004. Thermoelastic properties of $MgSiO_3$-perovskite: Insights on the nature of the Earth's lower mantle. Phys. Rev. Lett. 92, 018501.

Wentzcovitch, R., Tsuchiya, T., Tsuchiya, J., 2006. $MgSiO_3$ postperovskite at D'' conditions. P Natl Acad Sci Usa 103, 543–546.

Wookey, J., Kendall, J.M., 2007. Seismic anisotropy of post-perovskite and the lowermost mantle, in: Hirose, K., Brodholt, J., Lay, T., Yuen, D.A. (Eds.), Post-Perovksite: The Last Mantle Phase Transition. American Geophysical Union Geophysical Monograph 174, Washington, USA, pp. 171–189.

Wookey, J., Kendall, J.M., 2008. Constraints on lowermost mantle mineralogy and fabric beneath Siberia from seismic anisotropy. Earth Planet Sci Lett 275, 32–42.

Wookey, J., Kendall, J.M., Rumpker, G., 2005a. Lowermost mantle anisotropy beneath the north Pacific from differential S–ScS splitting. Geophys J Int 161, 829–838.

Wookey, J., Stackhouse, S., Kendall, J.M., Brodholt, J.P., Price, G.D., 2005b. Efficacy of the post-perovskite phase as an explanation for lowermost-mantle seismic properties. Nature 438, 1004–1007.

Wysession, M., Langenhorst, A., Fouch, M.J., Fischer, K.M., Al-Eqabi, G., Shore, P., Clarke, T., 1999. Lateral variations in compressional/shear velocities at the base of the mantle. Science 284, 120–125.

Wysession, M.E., Lay, T., Revenaugh, J., Williams, Q., Garnero, E.J., Jeanloz, R., Kellogg, L., 1998. The D'' discontinuity and its implications, in: Gurnis, M., Wysession, M.E., Knittle, E., Buffett, B.A. (Eds.), The Core–Mantle Boundary Region. American Geophysical Union, Washington, D.C., USA. Geodynamics Series, pp. 273–298.

Yamazaki, D., Karato, S., 2002. Fabric development in (Mg,Fe)O during large strain, shear deformation: implications for seismic anisotropy in Earth's lower mantle. Phys. Earth Planet. Inter. 131, 251–267.

Yamazaki, D., Karato, S., 2007. Lattice-preferred orientation of lower mantle materials and seismic anisotropy in the D'' layer, in: Post-Perovksite: The Last Mantle Phase Transition. American Geophysical Union, Washington, D.C., USA. Geophysical Monograph, pp. 69–78.

Yamazaki, D., Yoshino, T., Ohfuji, H., Ando, J., Yoneda, A., 2006. Origin of seismic anisotropy in the D'' layer inferred from shear deformation experiments on post-perovskite phase. Earth Planet Sci Lett 252, 372–378.

Figure and table captions

Figure 1: Transverse isotropy, or hexagonal symmetry, and wave propagation through such a medium. On the left, the rotational axis of symmetry is vertical, leading to vertical transverse isotropy (VTI). On the right, the axis is tilted away from the vertical, leading to tilted transverse isotropy (TTI), or simply a general case of transverse isotropy (TI). Waves within the plane of isotropy are split into orthogonal fast (blue) and slow (red) waves. The dip θ and azimuth a (the dip direction) of the plane of isotropy define the TTI orientation.

Figure 2: Shear wave splitting in an anisotropic medium. The unsplit incoming shear wave encounters the anisotropic medium, and is split into two orthogonal waves, fast (S_1, blue) and slow (S_2, red). The delay between the two is measured as δt, and the fast orientation in the ray frame (measured relative to the vertical) is ϕ'.

Figure 3: Representation of elasticity tensor by the variation of V_P and V_S with direction. The leftmost diagram explains the wave anisotropy plots on the right. The tensor in the three cartesian directions 1, 2 and 3 is represented by an upper hemisphere projection of the variation of wave speed with direction. The top of the projection is the 1-direction, left the 2-direction, and out of the page the 3-direction. At each point (each inclination from the 3-axis, i, and azimuth clockwise away from 1 in the 1–2 plane, a), V_P ($\mathrm{km\,s^{-1}}$) and δV_S (%) are shown by colour according to the scale at the bottom. On the δV_S plot, the orientation of the fast shear wave as projected onto the upper hemisphere is shown by the black ticks. Shown are the average C_{ij} for a selection of five kimberlites from Mainprice and Silver (1993), where the X-, Y- and Z-directions are oriented to the 1-, 2- and 3-directions respectively.

Figure 4: Raypaths of some of the body wave phases used to study D″ anisotropy.

Figure 5: Shear wave splitting parameters of SKS and S phases from upper mantle anisotropy. The two phases have slightly different slownesses, corresponding to a different incidence angle beneath the station. The upper hemisphere phase velocity plots, left, show the case of TI with a symmetry axis parallel to 1 (representing north). The 2-axis points west and 3 is up (out of the page). The elastic constants are those of Mainprice and Silver (1993) as shown in Figure 3, but with an imposed hexagonal symmetry. The circles at the centre of the δV_{S} plot show the range of incidence angles of SKS (red, innermost), S (blue, outermost) and ScS (black) phases at distances described in the text. The splitting parameters corresponding to these distances and backazimuths and a 250 km-thick layer are shown on the right for SKS (red) and S (blue). There is almost no variation in SKS, and for ϕ the two phases experience indistinguishable splitting. For δt, the largest difference is about 0.3 s, and within typical errors the two phases would exhibit the same splitting parameters. The parameters for ScS lie between the two other phases.

Figure 6: SH-SV traveltime analysis, Figure 5 from Garnero and Lay (1997). The authors examine shear waves travelling along the CMB beneath Alaska from two events in 1970 and 1973, at distances $90.0° \leqslant \Delta \leqslant 97.8°$. The onset of the S wave on the transverse component (SH) is around 4 s before that of the radial component (SV). Because there is minimal energy on the transverse component for the SKS arrival, it appears that negligible upper mantle anisotropy affects the signal. Hence the authors conclude that the two components have experienced different velocities in the lowermost mantle ($V_{\mathrm{SH}} > V_{\mathrm{SV}}$).

Figure 7: Summary of previous studies of D″ anisotropy. Numbered regions corresponding to Table 1 are shown in outline, plotted on top of a global tomographic model of V_{S} at 2750 km (Becker and Boschi, 2002) (colour indicates the variation away from PREM (Dziewonski and Anderson, 1981) as per the legend). Regions where the dominant signal is $V_{\mathrm{SH}} > V_{\mathrm{SV}}$ are shown in blue; those where $V_{\mathrm{SH}} < V_{\mathrm{SV}}$ are in purple. Where a region is shown with red and blue stripes, both situations have been seen, as well as isotropy. Yellow areas indicate regions where the orientation of an assumed TTI fabric has been determined: this symbol shows the dip direction of the plane of isotropy with a tick of varying length, as shown in the legend (longer is steeper dip). In regions where one azimuth of raypaths show fast directions which are not CMB-parallel or -perpendicular, they also have a dip symbol as for the TTI regions, with the long bar parallel to the ray path in D″. Regions with no fill show isotropy, and grey-filled regions show complex isotropy, either from SKS–SKKS differential splitting (see Table 1), or because no studies comparing V_{SH} to V_{SV} have been undertaken.

Figure 8: Average depth profile of $\xi = V_{\mathrm{SH}}^2/V_{\mathrm{SV}}^2$ from the SAW642AN model of Panning and Romanowicz (2006) (red) and S362WMANI of Kustowski et al. (2008) (blue). For SAW642AN The uppermost and lowermost mantle show $\xi > 1$, whilst most of the lower mantle is approximately isotropic. S362WMANI does not show the same dominant signal in D″.

Figure 9: Example of a shear wave splitting measurement, slightly modified from Supplementary Figure 3 of Nowacki et al. (2010). The measurement is made at FCC (Fort Churchill, Manitoba, Canada) on the ScS phase from an 645 km-deep earthquake beneath Brazil at 13:27 on 21 July, 2007, and pre-corrected for upper mantle anisotropy beneath the receiver. Panel A shows the original three-component seismogram, with the predicted ScS arrival time for a 1–D global velocity model, and the arrival itself. Second panel (B) shows the horizontal components when rotated to the fast orientation ϕ, as found in the analysis, before and after time-shifting the slow component forward by the delay time found in the analysis. Lower left (C) shows the fast and slow waves before (upper left) and after (upper right) shifting by δt. The lower subpanels show the horizontal particle motion before and after correction with the optimum $(\phi, \delta t)$. Last panel (D) shows the λ_2 surface (corresponding to misfit) in ϕ–δt space, with the optimum splitting parameters given by the blue cross, and surrounding 95 % confidence interval (thick contour). Subplots to the right show the result of cluster analysis (Teanby et al., 2004)—the single cluster shows this is a stable result.

Figure 10: Comparison of SH–SV traveltime analysis and shear wave splitting for a transversely isotropic (TI) medium. On the left (A), the plane of isotropy is shown by the grey circle, dipping at an angle from the horizontal. This defines the orientation of the anisotropy. The ray frame fast orientation of the split shear wave, ϕ', is controlled by the angle between the ray and the dip direction of the plane of isotropy, α, so that ϕ' is along the line of intersection between the plane of isotropy and the plane normal to the ray path. On the right (B) is shown the radial (R) and transverse (T) components of the split shear wave for various ϕ'. For all cases $\delta t = 1.5$ s, as shown by the dashed lines. Measuring the delay time directly on the two components only gives the correct amount and orientation of splitting for the special cases of $\phi' = 0°$ or $90°$. Within $\sim 15°$ of 0 or 90°, such measurements are still useful for detecting the presence of anisotropy, but do not provide much information about the symmetry. Slightly modified from Wookey and Kendall (2007).

Figure 11: Structure of $MgSiO_3$-perovskite and -post-perovskite. Yellow spheres are Mg ions; SiO_6 octahedra are shown in blue.

Figure 12: Proportions of phases present in the lower mantle for pyrolite and MORB compositions (after Ono and Oganov (2005) and Hirose (2006), and partly based on Trønnes (2010)). Yellow regions show aluminous phase regions, whilst grey regions show phases of silica. Sloping phase boundaries represent the range of depths over which the transition between the phases probably occurs. $Ca(Fe,Ti)_2O_4$-type Al-bearing phase refers to the uncertainty over the structure of the phase. Abbreviations are: Ca-pv: $CaSiO_3$-perovskite; pv: (Mg,Fe)(Si,Al)SiO_3-perovskite; ppv: (Mg,Fe)(Si,Al)SiO_3-post-perovskite; st: staurolite; α-PbO_2: SiO_2 in the α-PbO_2 form (also called columbite structure).

Figure 13: Elastic P and S wave anisotropy for pv from calculations at lower mantle conditions. (Top: Wookey et al. (2005b); bottom: Wentzcovitch et al. (2006).) Plots on the left show upper hemisphere, equal area projections of V_P with direction within the orthorhombic crystal. The 1, 2 and 3 axes are shown, corresponding to the [100], [010] and [001] directions respectively: 1 is up, 2 is left and 3 is out of the page. Colour indicates V_P as shown in the scale bar at the bottom. Plots on the right show δV_S (colour as per the scale bar) and the fast shear wave orientation with direction (black ticks). Because of the orthorhombic symmetry, each plot only varies within each quadrant.

Figure 14: Elastic P and S wave anisotropy for ppv from experiments and calculations at $T = 4000$ K (top to bottom: Stackhouse et al., 2005b; Wentzcovitch et al., 2006; Mao et al., 2010). Features as for Figure 13.

Figure 15: Elastic P and S wave anisotropy for fpc from *ab initio* calculations and experiment at lower mantle conditions. The three axes (1, 2 and 3) each corresponds to the $\langle 100 \rangle$ directions—because of the cubic symmetry the plots only vary within each eighth of the upper hemisphere.

Figure 16: Lattice preferred orientation (LPO) of crystals (A) and shape preferred orientation (SPO) of prolate (B) and oblate (C) slower isotropic inclusions in a faster anisotropic matrix (schematic). Spheres above are 3-D versions of the plots explained in Figure 3. They show the amount of shear wave anisotropy δV_S by colour, and the fast shear wave orientation by black ticks. Note that the colour scales are different. Blue arrows show a direction of flow which may align the crystals or inclusions, and thus how this might be interpreted from measuring the anisotropy.

Figure 17: Inferred TTI planes beneath the Caribbean, taken from Supplementary Information to Nowacki et al. (2010). The bar symbols show the direction of dip with the short tick, with the dip in degrees of the plane of isotropy given by the numbers. Beneath, colour shows the variation of V_S in the S20RTS model (Ritsema et al., 1999) at 2750 km depth. The coloured areas labelled 'W', 'S' and 'E' show the approximate horizontal region of sensitivity of ScS at 2750 km. Thin black lines show individual raypaths of ScS in the bottom 250 km of the mantle.

Figure 18: TTI plane of isotropy in region 'E' of Nowacki et al. (2010), shown by schematic layering of the material. Rays from South America travelling north show $\phi' \approx 90°$, whilst those from the Mid-Atlantic Ridge (MAR) travelling northwest exhibit $\phi' = 45°$. Assuming hexagonal symmetry where $\delta \approx \epsilon$, the fast orientation is in the plane of isotropy in each case. Whilst TTI is a possible explanation, it is only one type of anisotropy which can produce the observations with two azimuths of waves.

Figure 19: Shear wave anisotropy for horizontal (left) and inclined (right) melt inclusions in D″. The cartoons below show the alignment of oblate spheroids which respond to the motion of the mantle differently. In both cases, the sense of shear is top to the north (approximately right here), shown by the arrow. On the left, the inclusions are aligned parallel to the horizontal flow and produce VTI. On the right, the melt inclusions dip at 25° towards the sense of shear, opposite the sense of flow. For most azimuths of horizontally-propagating shear waves, this produces splitting with the fast orientation parallel to the alignment of the oblate inclusions. As discussed in the text, this is compatible with observations beneath Siberia and the Caribbean. The elastic constants are calculated using effective medium theory (Tandon and Weng, 1984) for an arbitrary set of lowermost mantle-like properties (matrix: $V_\mathrm{P} = 14$ km s^{-1}, $V_\mathrm{S} = 7.3$ km s^{-1}, $\rho = 5500$ kg m^3; inclusions: $V_\mathrm{P} = 7$ km s^{-1}, $V_\mathrm{S} = 0$ km s^{-1}, $\rho = 5500$ kg m^3, aspect ratio = 0.01, volume fraction = 0.005).

Figure 20: Variation of shear wave splitting with direction for $MgSiO_3$ post-perovskite (elastic constants of Stackhouse et al. 2005b at 3000 K). Colour indicates the strength of shear wave anisotropy in a given direction (δV_S) as per the scale bar. The black bars show the orientation of the fast shear wave. The crystallographic directions are indicated. (A) Shear wave splitting for unaltered single-crystal constants. There is strong ($\delta V_\mathrm{S} = 20\,\%$) anisotropy for rays along [100] and $\langle 111 \rangle$. (B) Anisotropy for a planar average of the constants when rotated around [001]. Strong ($\delta V_\mathrm{S} = 15\,\%$) splitting occurs within the plane normal to [001], with fast directions also in the plane. However, this corresponds to an aggregate of perfect alignment of [001] directions of pure ppv, which does not occur in D″.

Figure 21: Upper hemisphere diagrams showing shear planes and slip directions which are compatible with the measurements of sub-Caribbean D″ shear wave splitting of Nowacki et al. (2010). The schematic diagram on the left shows how to interpret the diagrams on the right: they show the upper hemisphere projection of the slip plane (coloured lines) and slip direction (black dots), hence the centre of the plots corresponds to the vertical direction; in this case the top of the diagrams is north. The elastic constants tested are those of Yamazaki et al. (2006), who deform ppv to produce an aggregate consistent with the dominant slip system in the crystal of [100](010). Three regions (‘W’, ‘S’ and ‘E’) are shown. Lighter colours show that more alignment of the phase via the slip system is required to produce the observed splitting—larger splitting times are observed in region S. For these constants, orientations of the shear plane dipping south or southeast can produce the observed splitting in regions S and E; horizontal shear can explain the splitting in region W.

Figure 22: Flow chart showing the progression of calculations and assumptions required to predict flow from measurements of shear wave splitting.

Table 1: Summary of previous studies of anisotropy in the lowermost mantle.

Table 2: Summary of inferred slip systems in $MgSiO_3$ post-perovskite and structural analogues from deformation experiments using the diamond-anvil cell (DAC), laser-heated diamond-anvil cell (LHDAC), Kawai-type and deformation-DIA (D-DIA) apparatuses.

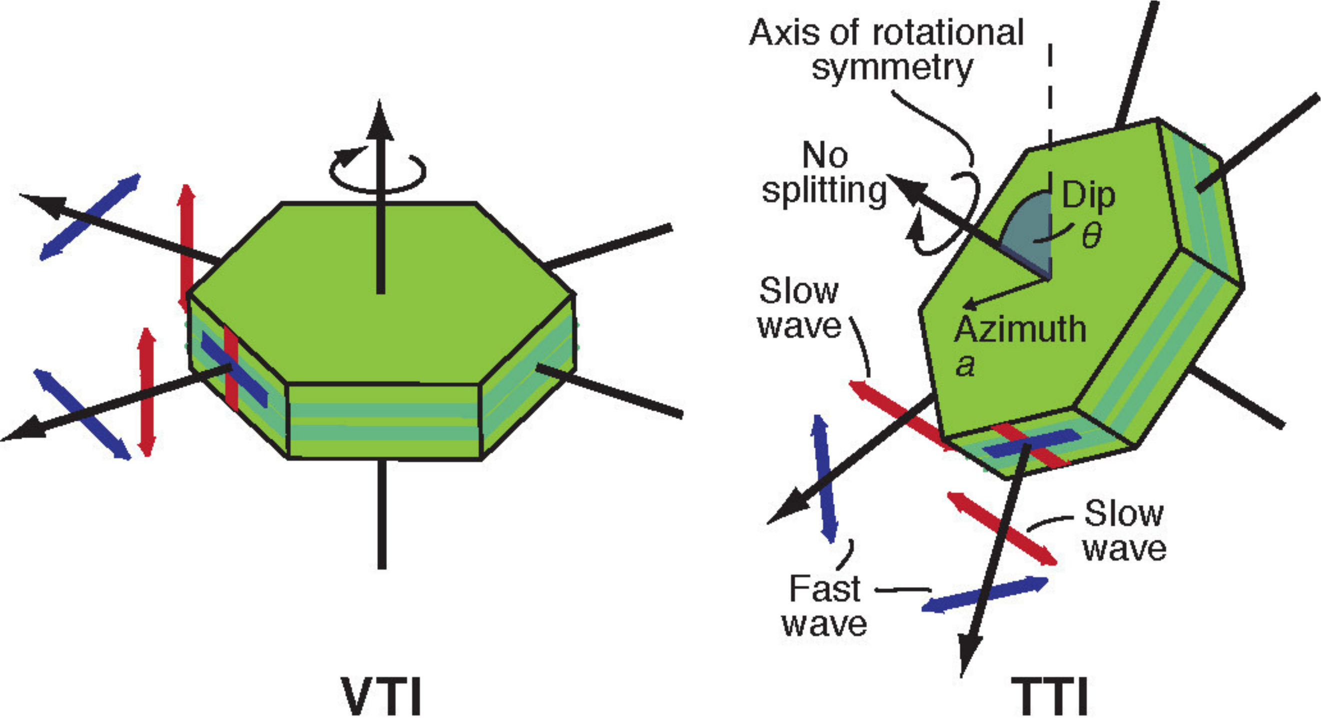

Axis of rotational symmetry
No splitting
Dip
θ
Azimuth
a
Slow wave
Slow wave
Fast wave
VTI
TTI

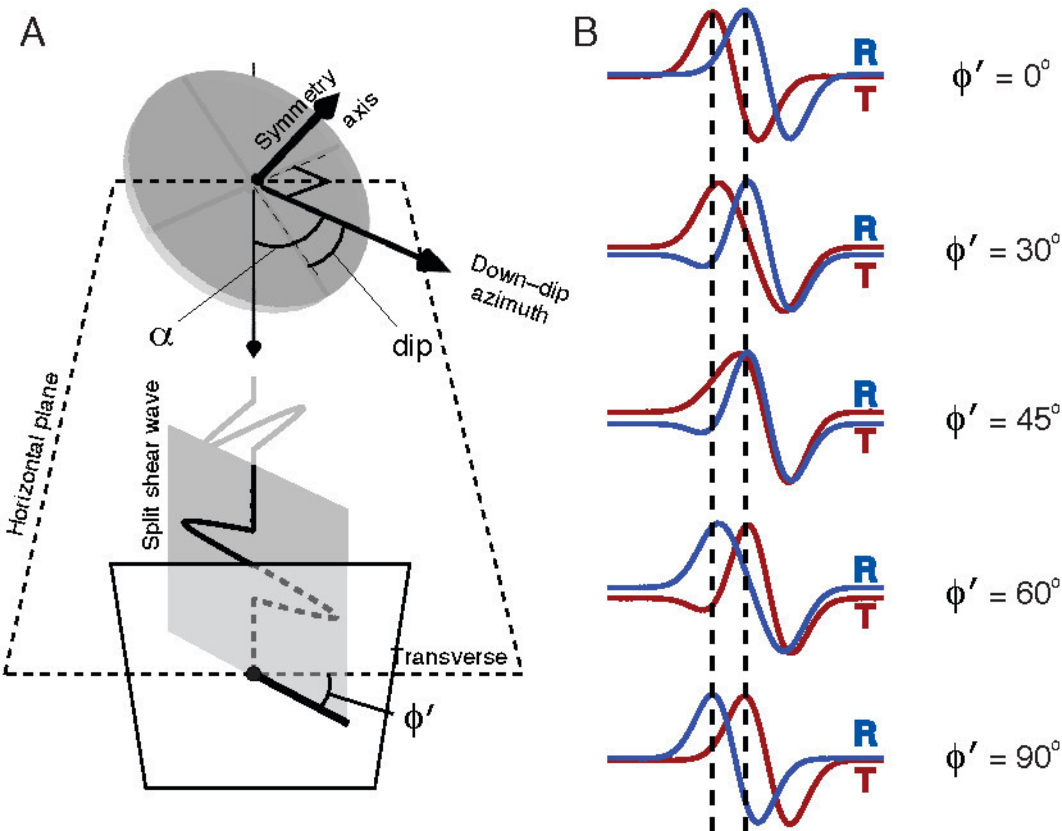

A
B
Symmetry axis
Down-dip azimuth
α
dip
Horizontal plane
Split shear wave
Transverse
φ′
R
T
φ′ = 0°
φ′ = 30°
φ′ = 45°
φ′ = 60°
φ′ = 90°

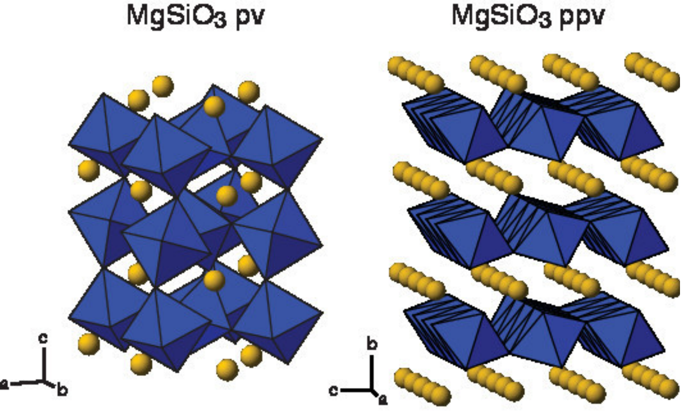

MgSiO$_3$ pv
MgSiO$_3$ ppv
c
a
b
b
c
a

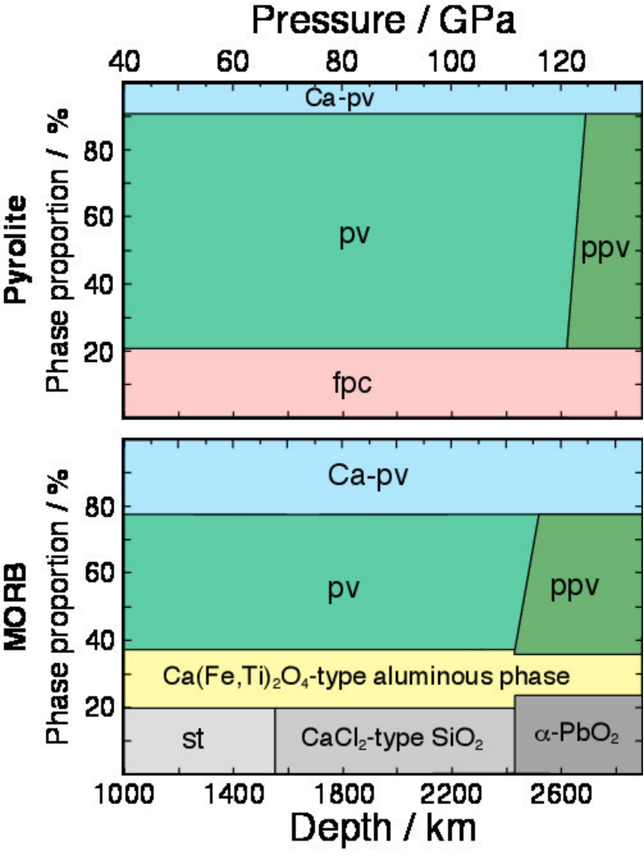
Pressure / GPa
40
60
80
100
120
Ca-pv
pv
ppv
fpc
Pyrolite
Phase proportion / %
80
60
40
20
Ca-pv
pv
ppv
Ca(Fe,Ti)$_2$O$_4$-type aluminous phase
st
CaCl$_2$-type SiO$_2$
α-PbO$_2$
MORB
Phase proportion / %
80
60
40
20
1000
1400
1800
2200
2600
Depth / km

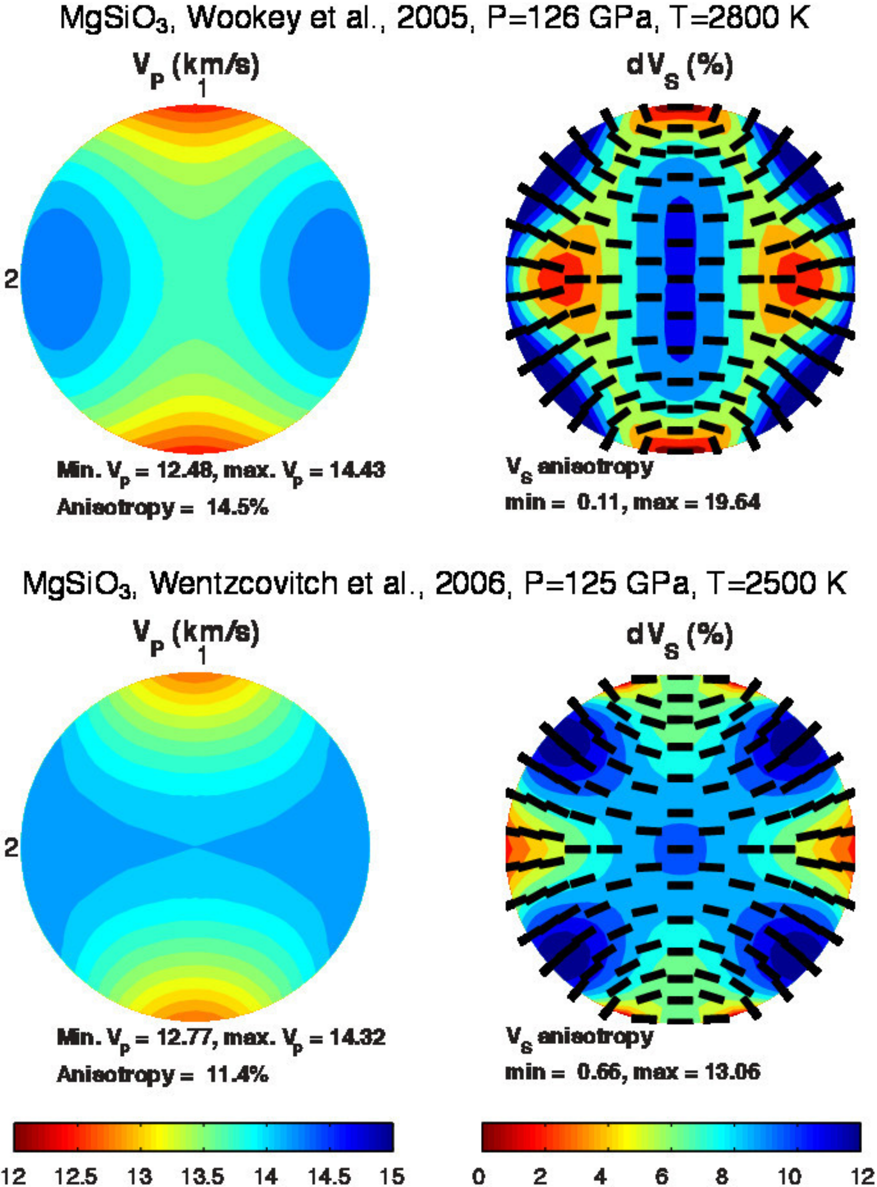
MgSiO3, Wookey et al., 2005, P=126 GPa, T=2800 K
VP (km/s)
1
2
dVS (%)
Min. Vp = 12.48, max. Vp = 14.43
Anisotropy = 14.5%
VS anisotropy
min = 0.11, max = 19.64
MgSiO3, Wentzcovitch et al., 2006, P=125 GPa, T=2500 K
VP (km/s)
1
2
dVS (%)
Min. Vp = 12.77, max. Vp = 14.32
Anisotropy = 11.4%
VS anisotropy
min = 0.66, max = 13.06
12 12.5 13 13.5 14 14.5 15
0 2 4 6 8 10 12

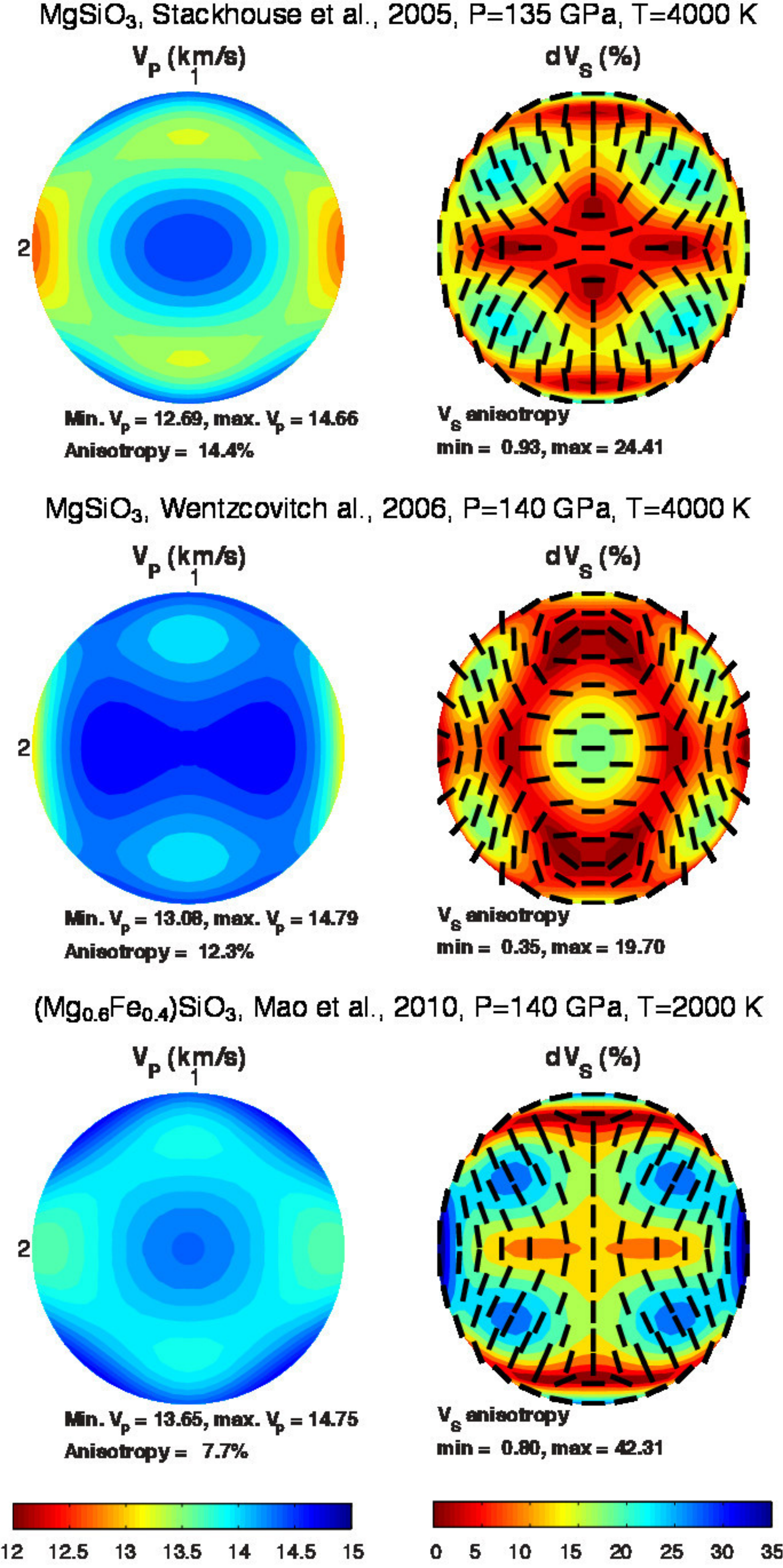
MgSiO3, Stackhouse et al., 2005, P=135 GPa, T=4000 K
Vp (km/s)
dVs (%)
1
2
Min. Vp = 12.69, max. Vp = 14.66
Anisotropy = 14.4%
Vs anisotropy
min = 0.93, max = 24.41
MgSiO3, Wentzcovitch al., 2006, P=140 GPa, T=4000 K
Vp (km/s)
dVs (%)
1
2
Min. Vp = 13.08, max. Vp = 14.79
Anisotropy = 12.3%
Vs anisotropy
min = 0.35, max = 19.70
(Mg0.6Fe0.4)SiO3, Mao et al., 2010, P=140 GPa, T=2000 K
Vp (km/s)
dVs (%)
1
2
Min. Vp = 13.65, max. Vp = 14.75
Anisotropy = 7.7%
Vs anisotropy
min = 0.80, max = 42.31
12 12.5 13 13.5 14 14.5 15
0 5 10 15 20 25 30 35

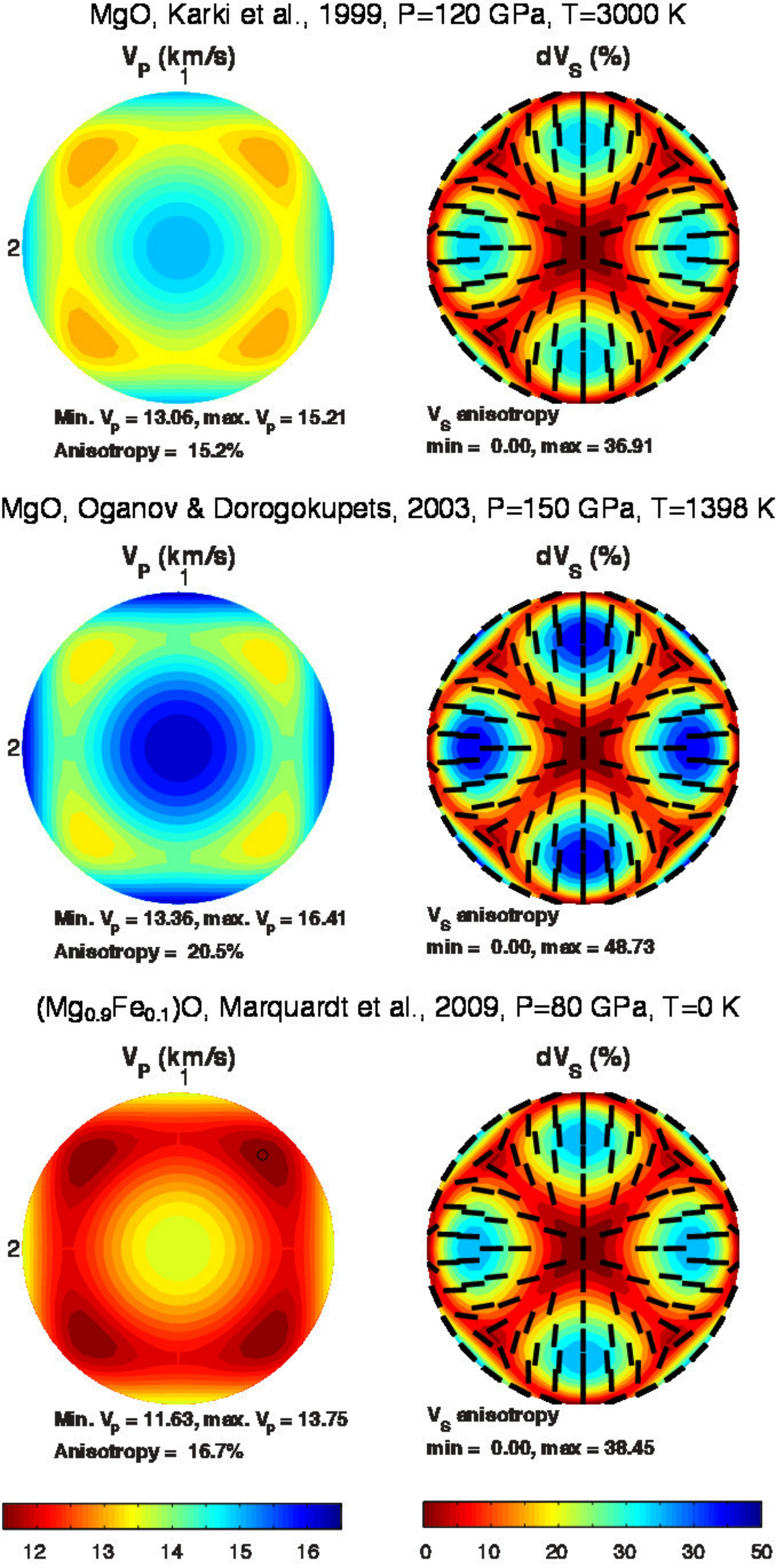

MgO, Karki et al., 1999, P=120 GPa, T=3000 K
Vp (km/s)
1
2
Min. Vp = 13.06, max. Vp = 15.21
Anisotropy = 15.2%
dVs (%)
Vs anisotropy
min = 0.00, max = 36.91
MgO, Oganov & Dorogokupets, 2003, P=150 GPa, T=1398 K
Vp (km/s)
1
2
Min. Vp = 13.36, max. Vp = 16.41
Anisotropy = 20.5%
dVs (%)
Vs anisotropy
min = 0.00, max = 48.73
(Mg0.9Fe0.1)O, Marquardt et al., 2009, P=80 GPa, T=0 K
Vp (km/s)
1
2
Min. Vp = 11.63, max. Vp = 13.75
Anisotropy = 16.7%
dVs (%)
Vs anisotropy
min = 0.00, max = 38.45
12 13 14 15 16
0 10 20 30 30 50

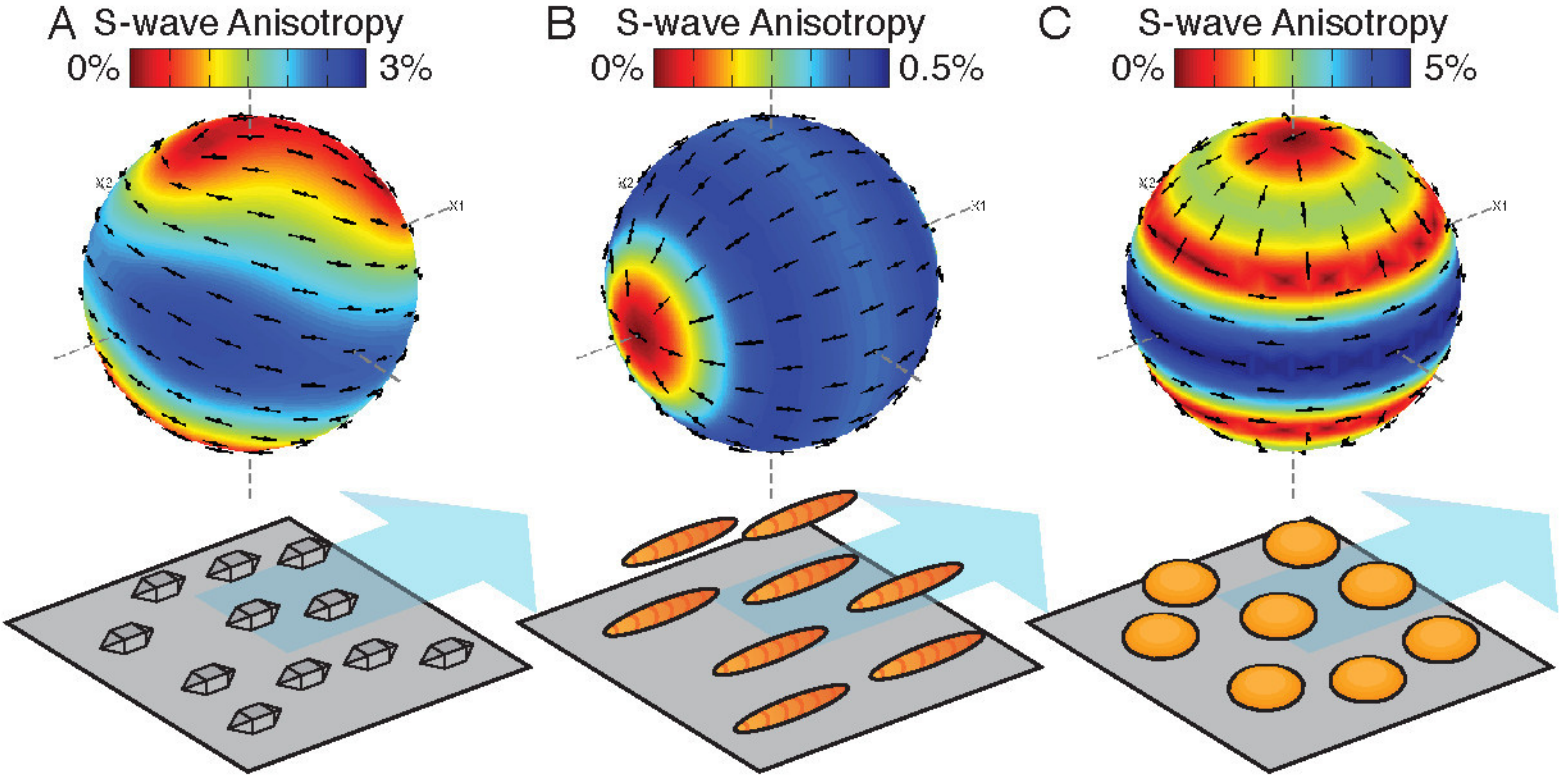

A S-wave Anisotropy
0%
3%
X2
X1
B S-wave Anisotropy
0%
0.5%
X2
X1
C S-wave Anisotropy
0%
5%
X2
X1

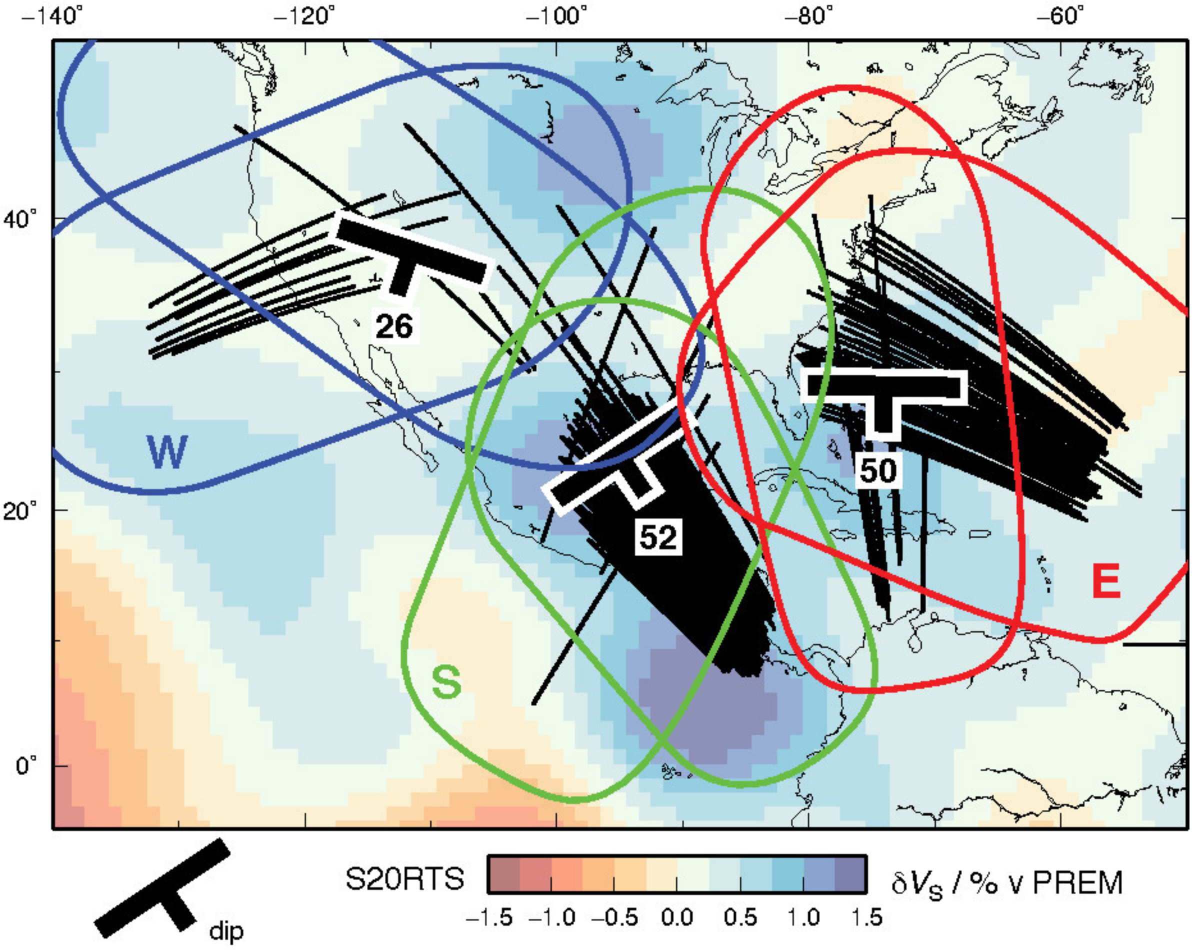

−140°
−120°
−100°
−80°
−60°
40°
20°
0°
26
52
50
W
S
E
dip
S20RTS
−1.5 −1.0 −0.5 0.0 0.5 1.0 1.5
δVS / % v PREM

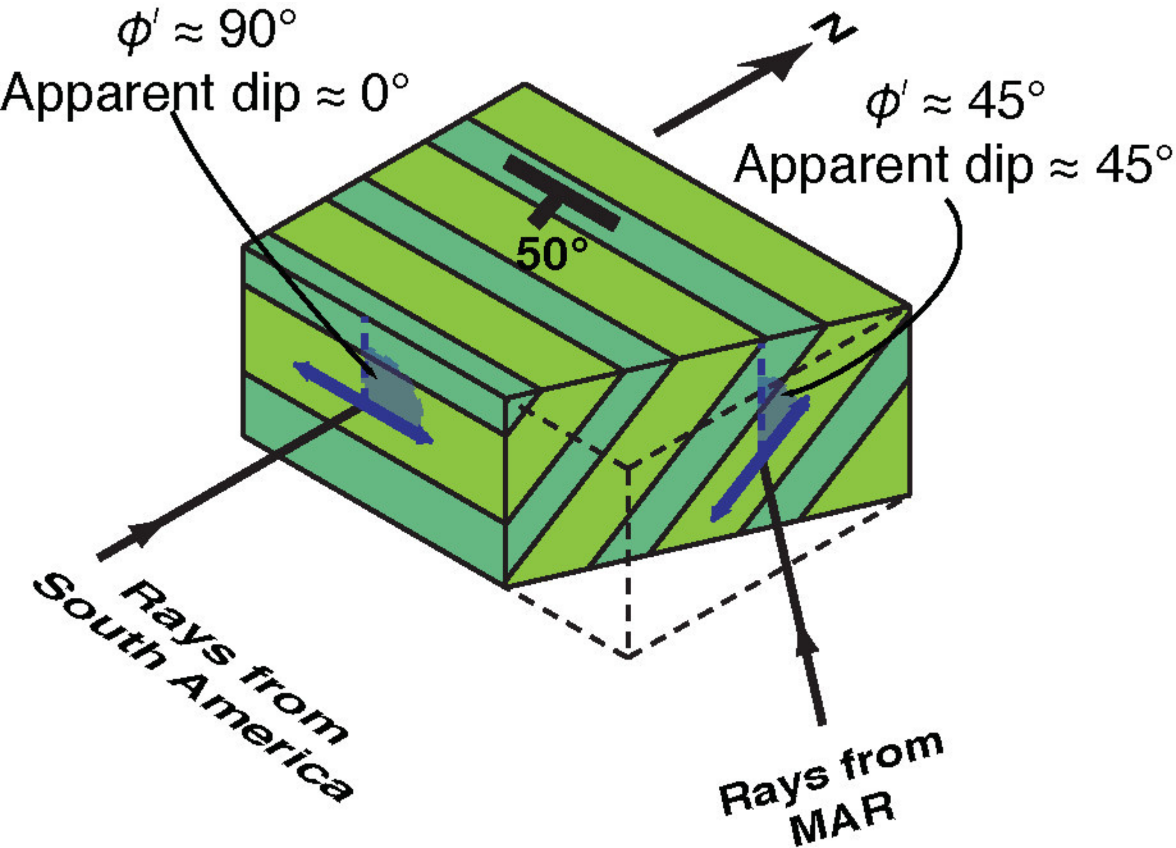

$\phi' \approx 90°$
Apparent dip ≈ 0°
N
$\phi' \approx 45°$
Apparent dip ≈ 45°
50°
Rays from
South America
Rays from
MAR

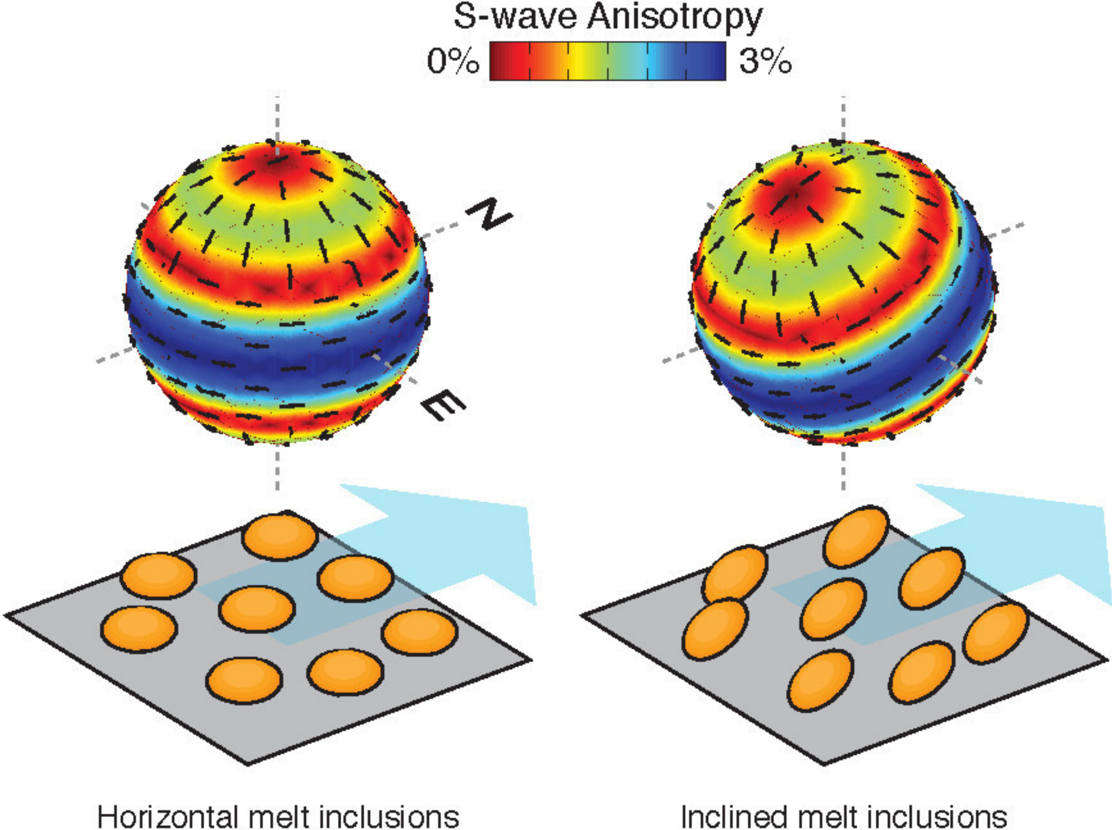
S-wave Anisotropy
0%
3%
N
E
Horizontal melt inclusions
Inclined melt inclusions

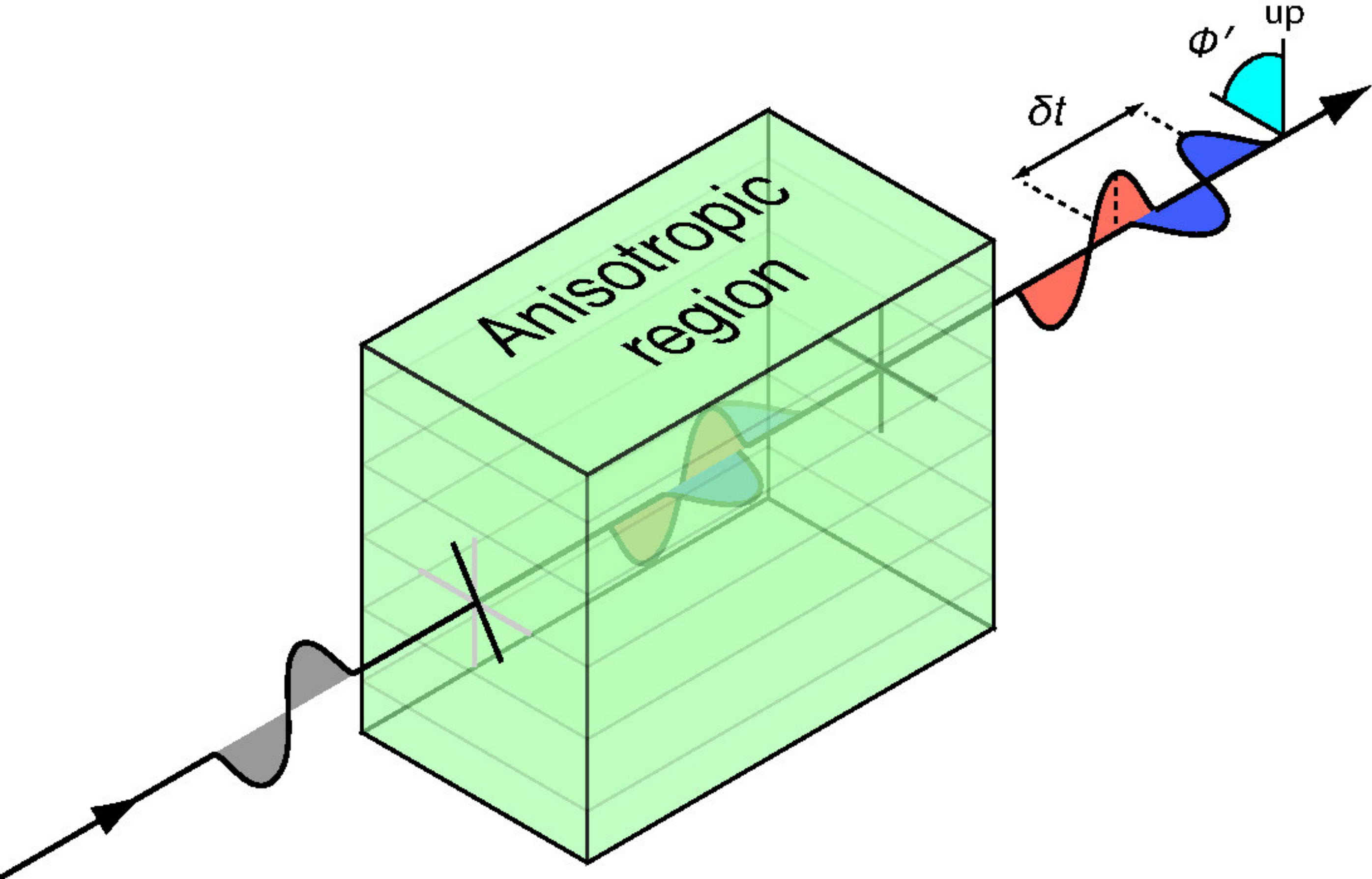

Anisotropic
region
δt
Φ′
up

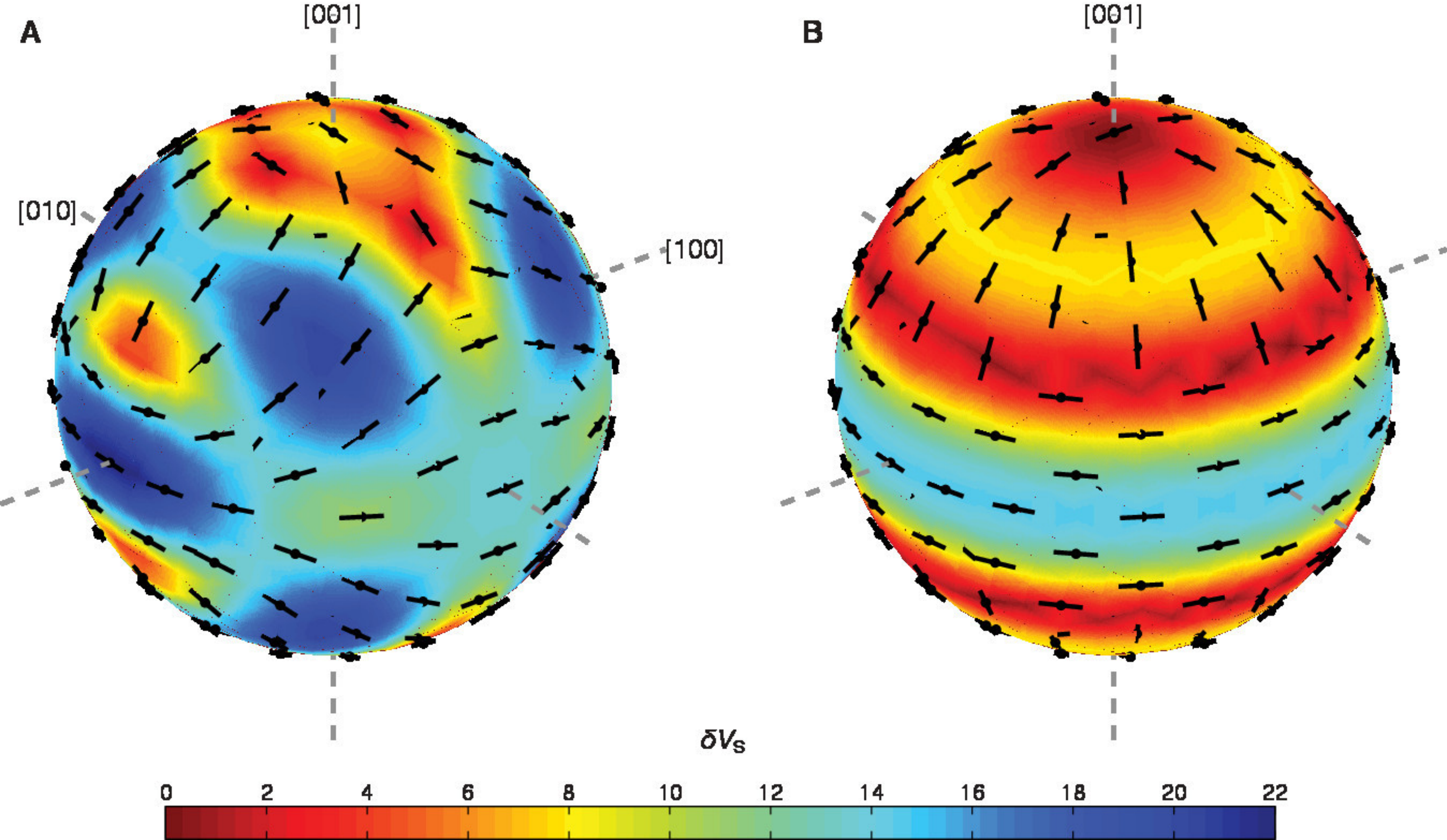

A
B
[001]
[001]
[010]
[100]
δV_S
0
2
4
6
8
10
12
14
16
18
20
22

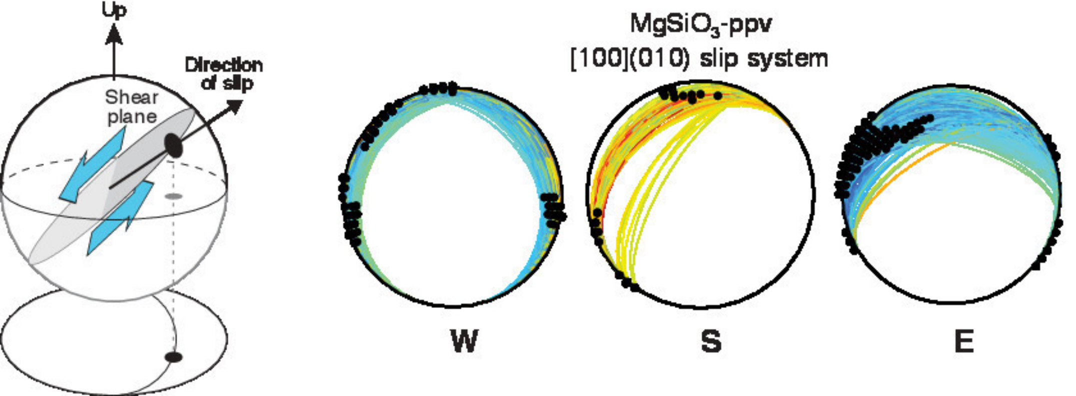
Up
Direction of slip
Shear plane
MgSiO$_3$-ppv
[100](010) slip system
W
S
E

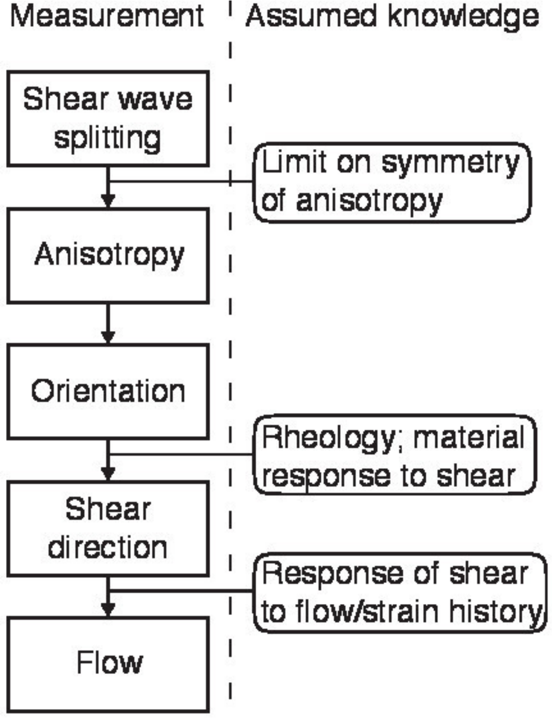
Measurement
Assumed knowledge
Shear wave splitting
Limit on symmetry of anisotropy
Anisotropy
Orientation
Rheology; material response to shear
Shear direction
Response of shear to flow/strain history
Flow

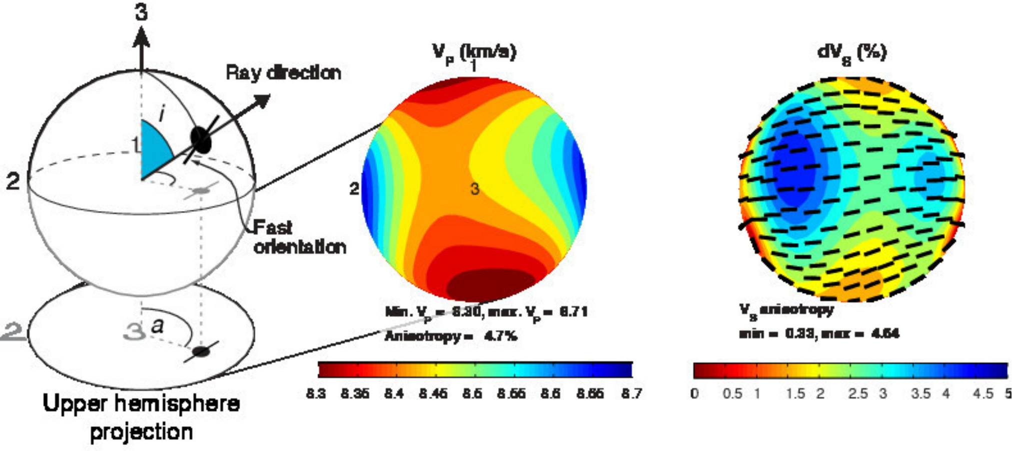

3
Ray direction
i
1
2
Fast orientation
2
3
a
Upper hemisphere projection
V_P (km/s)
1
2
3
Min. V_P = 8.30, max. V_P = 8.71
Anisotropy = 4.7%
8.3 8.35 8.4 8.45 8.5 8.55 8.6 8.65 8.7
dV_S (%)
V_S anisotropy
min = 0.33, max = 4.64
0 0.5 1 1.5 2 2.5 3 3.5 4 4.5 5

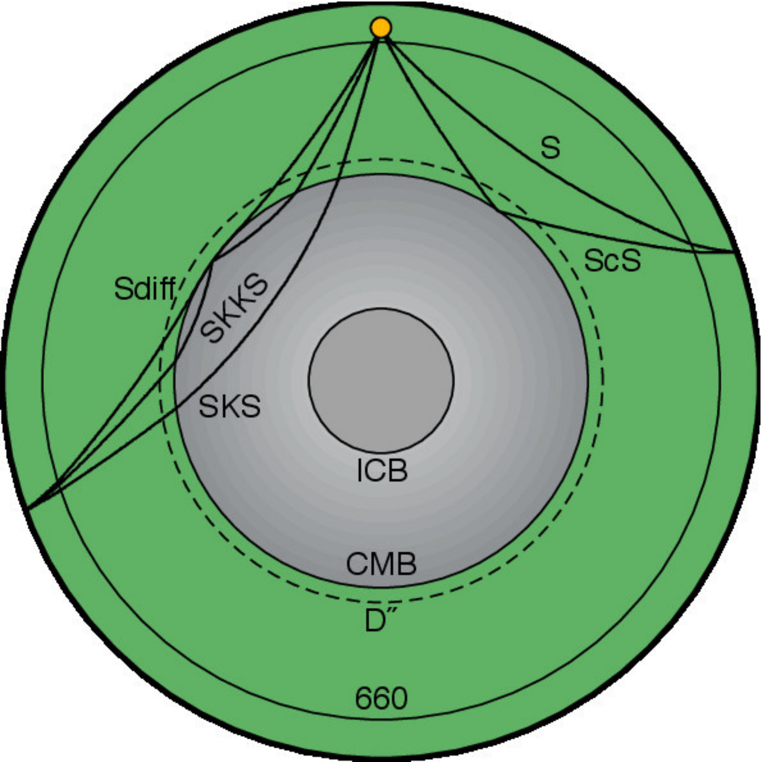
S
ScS
Sdiff
SKKS
SKS
ICB
CMB
D"
660

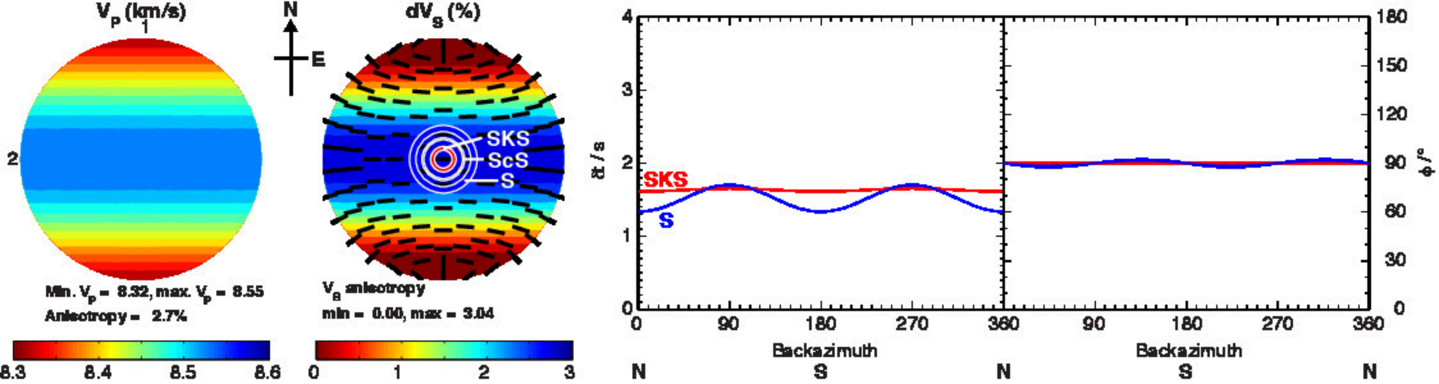

Vp (km/s)
1
2
N
E
dVs (%)
SKS
ScS
S
Min. Vp = 8.32, max. Vp = 8.55
Anisotropy = 2.7%
Vs anisotropy
min = 0.00, max = 3.04
8.3
8.4
8.5
8.6
0
1
2
3
δt / s
SKS
S
φ / °
Backazimuth
Backazimuth
N
S
N
S
N

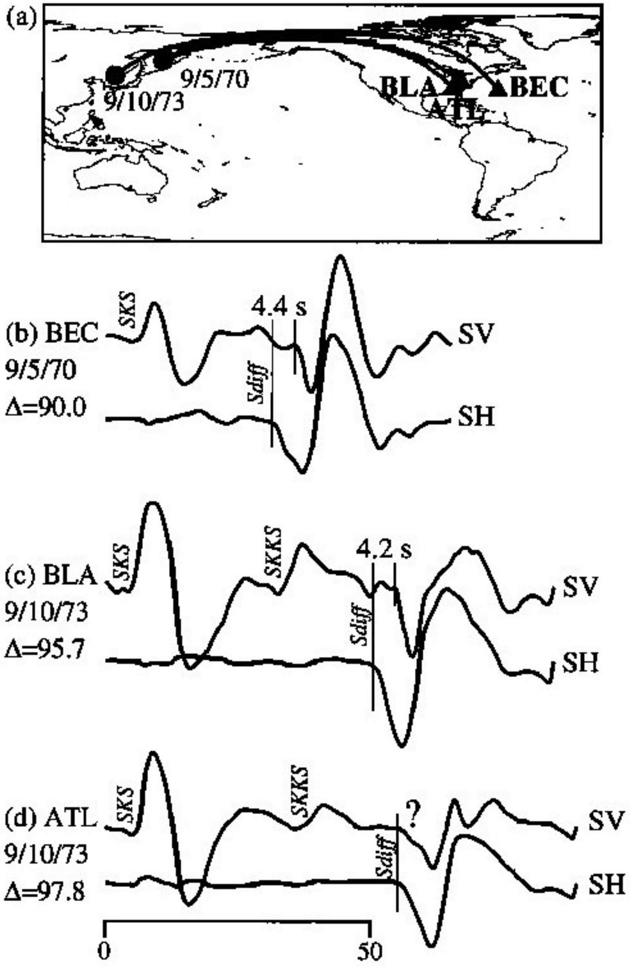

(a)
9/5/70
9/10/73
BLA
BEC
ATL
(b) BEC
9/5/70
Δ=90.0
SKS
4.4 s
Sdiff
SV
SH
(c) BLA
9/10/73
Δ=95.7
SKS
SKKS
4.2 s
Sdiff
SV
SH
(d) ATL
9/10/73
Δ=97.8
SKS
SKKS
?
Sdiff
SV
SH
0
50

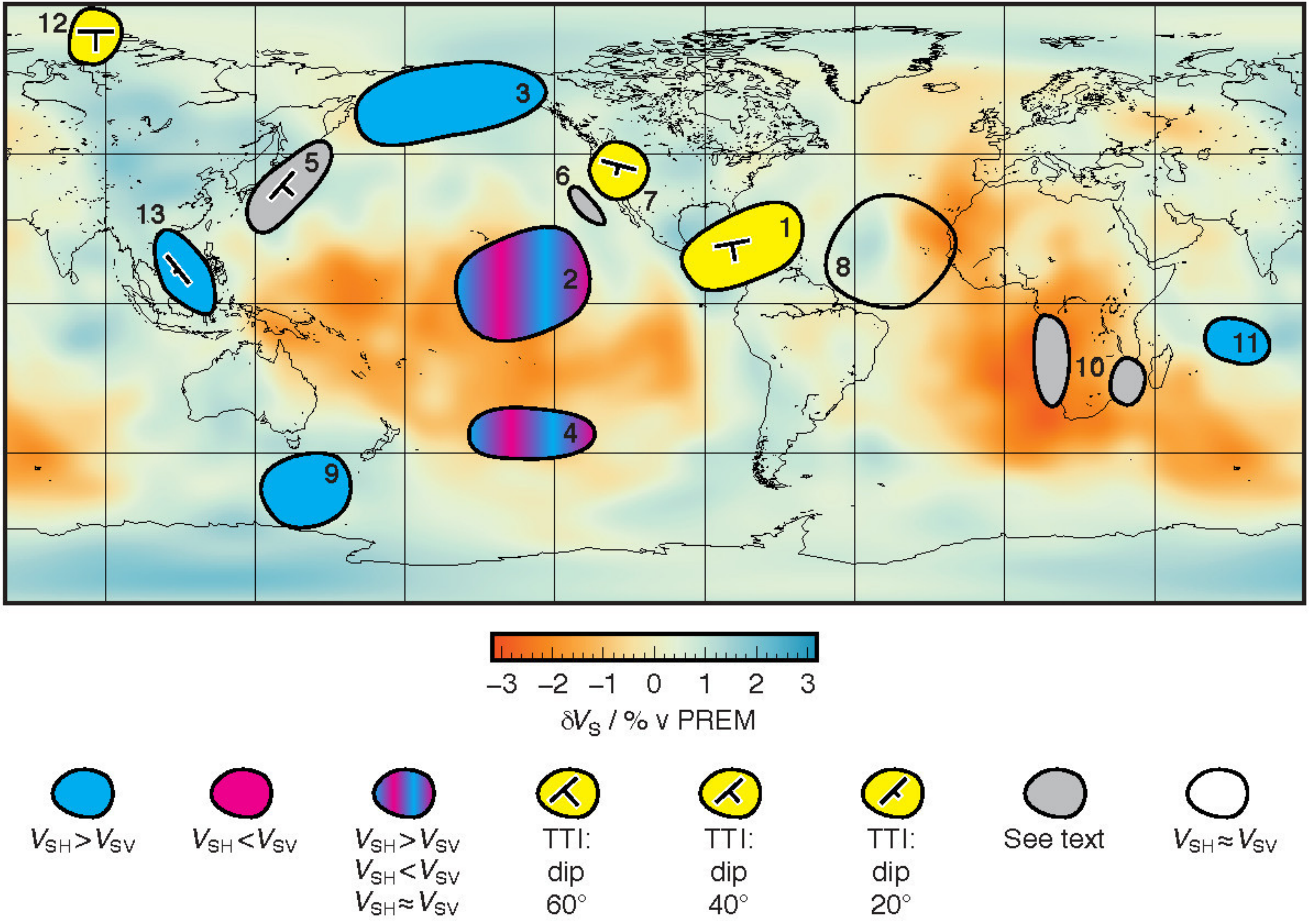

1
2
3
4
5
6
7
8
9
10
11
12
13
−3 −2 −1 0 1 2 3
δVS / % v PREM
VSH > VSV
VSH < VSV
VSH > VSV
VSH < VSV
VSH ≈ VSV
TTI: dip 60°
TTI: dip 40°
TTI: dip 20°
See text
VSH ≈ VSV

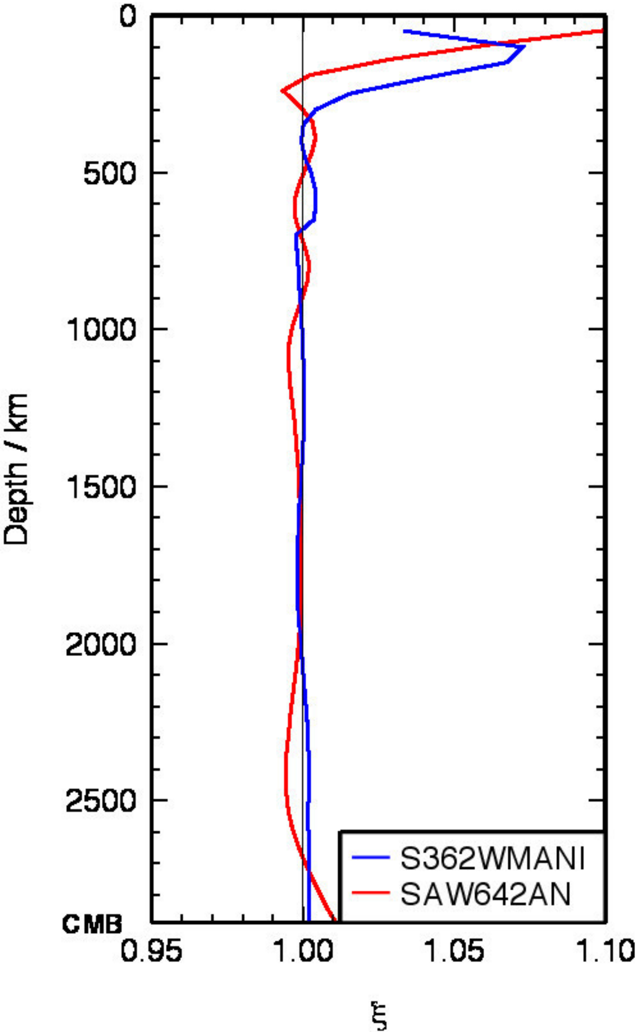

0
500
1000
1500
2000
2500
CMB
Depth / km
0.95
1.00
1.05
1.10
ξ
S362WMANI
SAW642AN

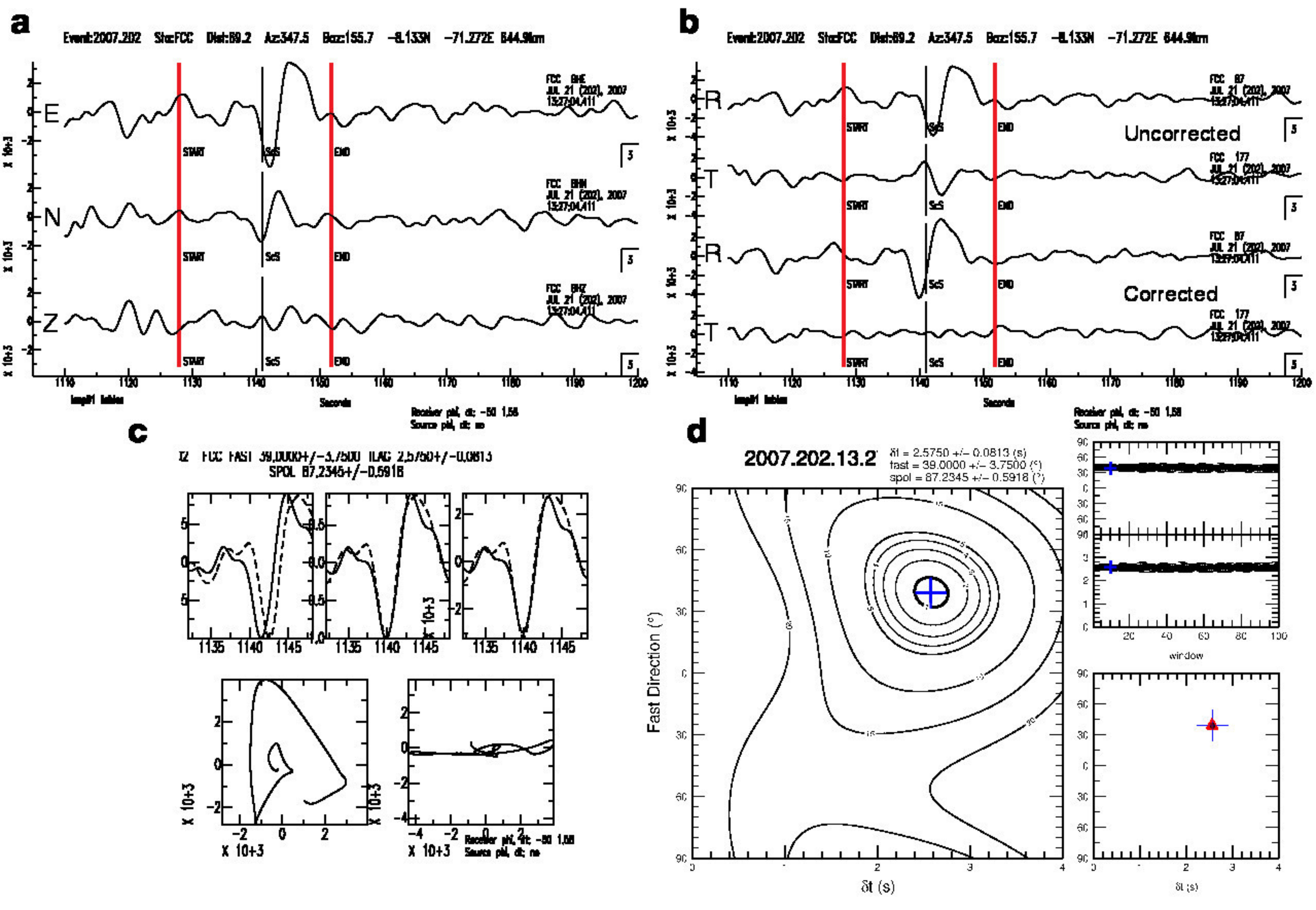
a
Event:2007.202 Sta:FCC Dist:89.2 Az:347.5 Baz:155.7 -8.133N -71.272E 644.9km
E
N
Z
START
ScS
END
Seconds
b
R
T
Uncorrected
Corrected
c
SPOL 87.2345+/-0.5918
d
2007.202.13.2
δt = 2.5750 +/- 0.0813 (s)
fast = 39.0000 +/- 3.7500 (°)
spol = 87.2345 +/- 0.5918 (°)
Fast Direction (°)
δt (s)
window

Table1

Table 1: Summary of previous studies of anisotropy in the lowermost mantle.

Study	Phases used	Observation	δV_S / %[a]	Suggested style of anisotropy
1. Caribbean				
Lay and Helmberger (1983)	ScS	$V_{SH} > V_{SV}$	5	Isotropic velocity structure
Kendall and Silver (1996)	S,Sdiff	$V_{SH} > V_{SV}$	1.8	VTI
Ding and Helmberger (1997)	ScS	$V_{SH} > V_{SV}$	2.5	VTI
Rokosky et al. (2004)	ScS	$V_{SH} > V_{SV}$	0.6	VTI
Garnero et al. (2004a)	S,ScS,Sdiff	$\leq 20°$ dip east-west		TTI
Maupin et al. (2005)	S,ScS,Sdiff	$\leq 20°$ dip east-west	1.5–2.2	TTI
Rokosky et al. (2006)	ScS	Mostly $V_{SH} > V_{SV}$	0.0–2.0[b,c]	Varying TTI
Nowacki et al. (2010)	ScS	~50° dip ~south	0.8–1.5	TTI or orthorhombic
2. Central Pacific				
Vinnik et al. (1995)	Sdiff	$V_{SH} > V_{SV}$	0.6[b]	VTI
Vinnik et al. (1998)	Sdiff	$V_{SH} > V_{SV}$	~10	VTI
Pulliam and Sen (1998)	S	$V_{SH} < V_{SV}$	−2	VTI
Ritsema et al. (1998)	S,Sdiff	$V_{SH} < V_{SV}$	−2.1–−1.4	VTI
Kendall and Silver (1998)	S,Sdiff	$V_{SH} \approx V_{SV}$		Isotropic
Russell et al. (1998, 1999)	ScS	$V_{SH} > V_{SV}, V_{SH} < V_{SV}$	2–3	VTI
Fouch et al. (2001)	S,Sdiff	$V_{SH} > V_{SV}$	0.3–5.3	VTI
Kawai and Geller (2010)	S,ScS,SKS	$V_{SH} < V_{SV}$	−3	VTI
3. Alaska				
Lay and Young (1991)	S,ScS,Sdiff	$V_{SH} > V_{SV}$		VTI
Matzel et al. (1996)	S,ScS,Sdiff	$V_{SH} > V_{SV}$	1.5–3	VTI
Garnero and Lay (1997)	S,ScS,Sdiff	Mainly $V_{SH} > V_{SV}$	−1–3	VTI
Wysession et al. (1999)	Sdiff	$V_{SH} > V_{SV}$	0.2–0.6	VTI or TTI
Fouch et al. (2001)	S,Sdiff	$V_{SH} > V_{SV}$	0–0.9	VTI
4. South East Pacific				
Ford et al. (2006)	S,Sdiff	$V_{SH} > V_{SV}, V_{SH} < V_{SV}$	−1.0–0.9	VTI
5. North West Pacific				
Wookey et al. (2005a)	ScS	~40° dip southeast	0.8–2.3	TTI
6. East Pacific				
Long (2009)	SKS-SKKS	Differential $\delta t \approx 2$ s [d]	0.5[b]	TTI
7. Western USA				
Nowacki et al. (2010)	ScS	26° dip southwest	1.2	VTI or TTI
8. Atlantic Ocean				
Garnero et al. (2004b)	S,Sdiff	$V_{SH} \approx V_{SV}$	≤ 0.5	Isotropy or weak VTI
9. Antarctic Ocean				
Usui et al. (2008)	S	$V_{SH} > V_{SV}$	1[b]	VTI
10. Southern Africa				
Wang and Wen (2007)	SKS-SKKS	Differential $\delta t \approx 1$ s [d]	~2[b]	Varying HTI
11. Indian Ocean				
Ritsema (2000)	S	$V_{SH} > V_{SV}$	1.4–1.7	VTI
12. Siberia				
Thomas and Kendall (2002)	S,ScS,Sdiff	Mainly $V_{SH} > V_{SV}$	−0.8–1.4	Mainly VTI
Wookey and Kendall (2008)	ScS	55° dip ~south	0.7–1.4	TTI or othorhombic
13. Southeast Asia				
Thomas et al. (2007)	ScS	9° dip southwest	0.5	VTI or TTI

[a] +ve: $V_{SH} > V_{SV}$; −ve: $V_{SH} < V_{SV}$

[b] Calculated from the study's stated δt using $\langle V_S \rangle$ from a global isotropic V_S model (Ritsema et al., 1999) for a uniform 250 km thick D″ layer.

[c] Upper limit on δt of 2.5 s imposed.

[d] Differential δt refers to $\delta t_{SKKS} - \delta t_{SKS}$.

Table 2: Summary of inferred slip systems in $MgSiO_3$ post-perovskite and structural analogues from deformation experiments using the diamond-anvil cell (DAC), laser-heated diamond-anvil cell (LHDAC), Kawai-type and deformation-DIA (D-DIA) apparatuses.

Study	Method	P (GPa)	T (K)	Differential stress (GPa)	Dominant slip system[a]	Remarks
			$(Mg,Fe)SiO_3$			
Merkel et al. (2007)	LHDAC	145–157	1800	7–9	(100) or (110)	Mg#=0.9; opx starting material
Miyagi et al. (2010)	LHDAC	148–185	3500	5–10	[100](001) or [010](001)	Mg#=1.0; glass starting material
Mao et al. (2010)	LHDAC	140	2000	[b]	{100} or {110}	Mg#=0.6; opx starting material
			$CaIrO_3$			
Yamazaki et al. (2006)	Kawai	1	1173		[100](010)	γ=0.4–1 [c]
Walte et al. (2007)	D-DIA	3	1000	[b]	[100](010)	γ=0.8–1
Niwa et al. (2007)	DAC	0–6	300	[b]	(010)	
Miyagi et al. (2008)	D-DIA	2–6	300–1300	−2–2	[100](010)	
Walte et al. (2009)	D-DIA	1-3	1300	[b]	[100]{010}	γ=0.5–1
			$MgGeO_3$			
Merkel et al. (2006)	LHDAC	104–124	1600	3–8	(100) or (110)	opx starting material
Kubo et al. (2008)	LHDAC	83–99	1600	0.1–1	(010)	opx starting material
Okada et al. (2010)	LHDAC	78–110	300	1–3	(001)	4 runs: opx and pv starting material
			$MnGeO_3$			
Hirose et al. (2010)	LHDAC	77–111	2000	2–10	(001)	opx starting material

[a] Where no slip vector is given in the study, only the slip plane is shown.
[b] Not stated.
[c] Shear strain γ as stated in the study.